male WT and Glp-1r$^{-/-}$ mice. Although the bone volume (BV)/tissue volume (TV) ratio (Fig. 2C) was somewhat lower in Glp-1r$^{-/-}$ mice in both tibia and spine, the difference was not statistically significant. The number of osteoclasts (N.Oc), especially multinuclear osteoclasts (N.Mu.Oc), the fully differentiated cells responsible for active bone resorption, was significantly increased in tibia of Glp-1r$^{-/-}$ mice (Fig. 2, D and E), and all of the following parameters indicating osteoclastic number were also significantly higher in the tibia of Glp-1r$^{-/-}$ mice: N.Mu.Oc per bone surface (BS) (2.06/mm^2 *vs.* 3.90/mm^2, $P = 0.022$), N.Mu.Oc per eroded surface (ES) (6.18/mm^2 *vs.* 9.32/mm^2, $P = 0.040$), N.Mu.Oc/TV (12.22/mm^2 *vs.* 20.26/mm^2, $P = 0.012$), N.Oc/BS (3.21/mm^2 *vs.* 5.98/mm^2, $P = 0.002$), and N.Oc/TV (19.28/mm^2 *vs.* 31.59/mm^2, $P = 0.009$), for WT *vs.* Glp-1r$^{-/-}$ mice, respectively. Furthermore, eroded surface (ES/BS) was significantly increased in the tibiae of Glp-1r$^{-/-}$ mice compared with WT mice (Fig. 2F). However, osteoclastic bone resorption activity was less apparent in spine of Glp-1r$^{-/-}$ mice (Fig. 2, E and F). On the other hand, no significant difference was observed in bone formation parameters, including osteoblast surface per BS (Fig. 2G), mineral apposition rate (Fig. 2H), and bone formation rate (Fig. 2I) between WT and Glp-1r$^{-/-}$ mice.

GLP-1 has no direct effect on osteoclasts and osteoblasts

Because osteoclastic number and bone resorptive activity were increased in Glp-1r$^{-/-}$ mice, we investigated whether GLP-1 has a direct effect on osteoclasts and/or osteoblasts using cell culture models. We first evaluated the effect of GLP-1 on osteoclastic differentiation by culturing bone marrow cells together with osteoblasts, because osteoclasts are formed from the precursor cells in bone marrow by stimulation from osteoblasts. As a result, GLP-1 had no inhibitory effect on 1α,25-dihydroxyvitamin D_3-induced osteoclastic generation (Fig. 3A). Pit-forming assays showed that GLP-1 had no direct effect on pit-forming activity of mature osteoclasts placed on dentine slices, whereas calcitonin completely inhibited pit formation (Fig. 3B). Unlike the GIP receptor, the GLP-1 receptor was absent in osteoblasts, and GLP-1failed to increase intracellular cAMP levels in Saos-2 cells (data not shown). Furthermore, GLP-1 had no protective effect on etoposide-induced osteoblastic apoptosis (Fig. 3C). These *in vitro* experiments demonstrate that GLP-1 has no direct effect on either osteoclasts or osteoblasts.

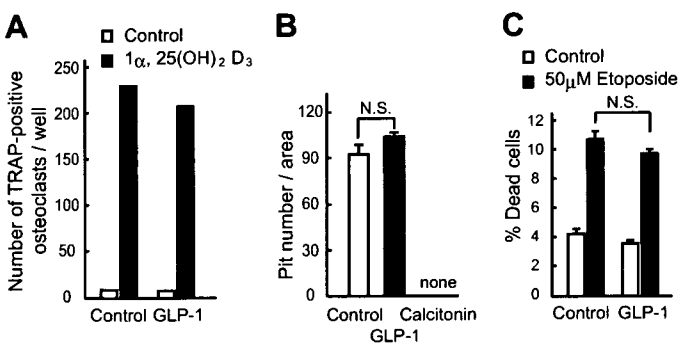

FIG. 3. Effects of GLP-1 on osteoclasts and osteoblasts *in vitro*. A, Effect of GLP-1 on osteoclastic differentiation. The numbers of tartrate-resistant acid phosphatase (TRAP)-positive osteoclasts formed from coculture of osteoblasts and bone marrow cells in the presence or absence of 10^{-8} M 1α,25-dihydroxyvitamin D_3 [1α, 25(OH)$_2$ D_3] (*white bars*)and/or 10^{-5} M GLP-1 (*black bars*) are shown. B, Effect of GLP-1 on the pit-forming activity of mature osteoclasts, using 10^{-10} M calcitonin as a positive control. C, Effect of GLP-1 on osteoblastic apoptosis. Saos-2 cells were pretreated with 10^{-4} M GLP-1 for 1 h and then incubated for an additional 6 h in the absence (*white bars*) or presence of 50 μM etoposide (*black bars*). Values are expressed as means ± SE.

GLP-1 receptor signaling modulates calcitonin expression in mice

Because GLP-1 has no direct effect on bone cells, we investigated indirect pathways of GLP-1-mediated bone metabolism. Plasma levels of total calcium (data not shown) and ionized calcium (Fig. 4A) were unchanged in both fasting and fed conditions. Because hyperparathyroidism is a cause of cortical bone loss, plasma intact PTH levels were measured, but there was no difference in PTH levels between WT and Glp-1r$^{-/-}$ mice (Fig. 4B). Because the GLP-1 receptor is expressed in thyroid C cells and GLP-1 stimulates calcitonin secretion *in vitro* via a cAMP-mediated mechanism (10, 11), calcitonin could be involved in the alteration of bone metabolism observed in Glp-1r$^{-/-}$ mice. Quantitative real-time PCR analysis revealed that administration of the GLP-1 receptor agonist exendin-4 significantly increased thyroid calcitonin mRNA levels in WT mice (Fig. 4C). Conversely, the loss of GLP-1 receptor signaling in Glp-1r$^{-/-}$ mice was as-

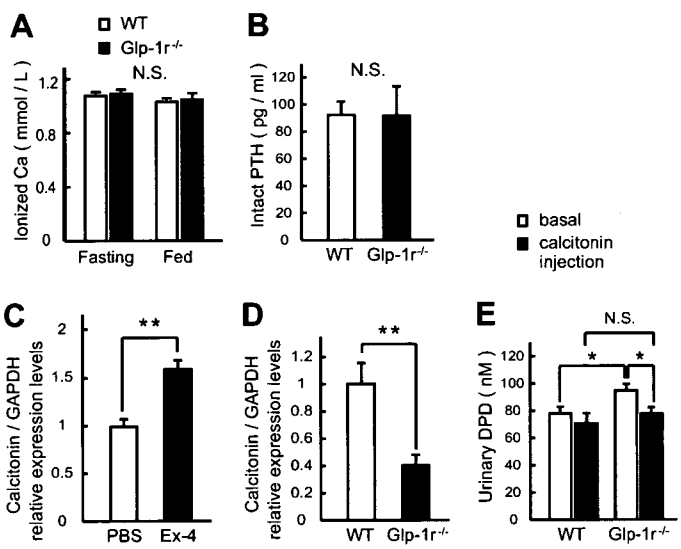

FIG. 4. Calcitonin deficiency resulted in increased bone resorption in Glp-1r$^{-/-}$ mice. A and B, Plasma levels of ionized calcium (A) and intact PTH (B) in WT and Glp-1r$^{-/-}$ mice. Values are expressed as means ± SE; n = 6–8 mice per group. C, Relative expression levels of calcitonin mRNA in thyroid from WT mice injected ip with PBS or 24 nmol/kg exendin-4 (Ex-4) 6 h before RNA isolation. Values are expressed as means ± SE; n = 5 mice per group. *, $P < 0.01$, PBS *vs.* exendin-4 treatment. D, Relative expression levels of calcitonin mRNA in thyroid from WT and Glp-1r$^{-/-}$ mice determined by quantitative real-time PCR. Values are expressed as means ± SE; n = 4 mice per group. *, $P < 0.05$; **, $P < 0.01$, WT *vs.* Glp-1r$^{-/-}$ mice. E, Urinary elimination of DPD from WT and Glp-1r$^{-/-}$ mice before and at 4 h after single administration of 10 IU/kg calcitonin. Values are expressed as means ± SE; n = 6 mice per group. *, $P < 0.05$, WT *vs.* Glp-1r$^{-/-}$ mice.

sociated with a significant reduction in levels of calcitonin mRNA transcripts, 41% of levels in control WT thyroid glands (Fig. 4D). Consistent with results of bone histomorphometry showing increased osteoclastic bone resorption, Glp-1r$^{-/-}$ mice showed significantly higher urinary DPD concentration (Fig. 4E). However, calcitonin treatment effectively decreased the urinary DPD concentration in Glp-1r$^{-/-}$ mice (Fig. 4E), demonstrating that increased bone resorption in Glp-1r$^{-/-}$ mice remains sensitive to the antiresorptive actions of calcitonin.

Discussion

Decreased BMD is a major determinant of fracture, but fracture risk in diabetic patients is often increased (17–19) and is not necessarily associated with decreased BMD. BMD in type 2 diabetes has been reported to be decreased, normal, or increased depending on various factors such as body weight or the site where BMD is measured. Body weight is one of the main determinants of BMD in both diabetic and nondiabetic subjects, suggesting that the increased BMD could be explained by the higher body weight. In the present study, there was no difference in several metabolic factors that often indirectly modulate BMD, including body weight, fat mass, or plasma levels of leptin, between WT and Glp-1r$^{-/-}$ mice.

Quantitative CT was used in the present study for the measurement of BMD because of the merits of the method with regard to distinct assessment of cortical, cancellous, and trabecular bones and to providing indexes of bone strength in live animals (13, 20). We found that total BMD of tibia, which has a higher cortical/cancellous bone ratio, was significantly lower in Glp-1r$^{-/-}$ mice and that cortical BMD at both tibia and lumbar spine was selectively reduced in Glp-1r$^{-/-}$ mice compared with WT mice. Reflecting the cortical bone loss, Glp-1r$^{-/-}$ mice showed skeletal fragility. In diabetic patients, BMD measured at sites with high cortical/cancellous bone ratio, such as distal radius or metacarpal bone, has been reported to be selectively decreased compared with sites high in cancellous bone such as lumbar spine or femoral neck (21–24). Reduced GLP-1 secretion is one of the features of type 2 diabetes (9), and it is of interest that cortical bone loss is observed in Glp-1r$^{-/-}$ mice as well as in diabetic patients. Therefore, we suppose that modulation of GLP-1 receptor signaling may theoretically contribute to regulation of bone turnover in diabetic subjects, a hypothesis that requires further testing.

We found by bone histomorphometry that genetic loss of GLP-1 receptor signaling resulted in significantly increased osteoclastic bone resorption activity, whereas the effects on bone formation parameters were less marked, similar to the changes in bone turnover induced by gastrointestinal factors. However, unlike GIP, GLP-1 had no direct effects on osteoclasts and osteoblasts as shown by the *in vitro* experiments.

Calcitonin is a known inhibitor of bone resorption and has been reported to prevent or retard bone loss in animal models of excessive bone resorption (25–28). As to the effect of calcitonin on cortical bone, calcitonin treatment has been shown to increase lumbar vertebral cortical thickness (29) and femoral cortical areas (30) in ovariectomized rats. It has been reported that the GLP-1 receptor is expressed in thyroid C cells and that GLP-1 stimulates calcitonin secretion via a cAMP-mediated mechanism in cultured C cells (10, 11); we also found that GLP-1 has a stimulatory effect on calcitonin gene expression in thyroid C cells *in vivo*, because attempts at measurement of plasma calcitonin were not successful due to sample volumes and assay sensitivity. Thus, increased osteoclastic bone resorption in Glp-1r$^{-/-}$ mice might arise indirectly from loss of GLP-1 receptor signaling on C cells, leading to calcitonin deficiency. Consistent with this hypothesis, Glp-1r$^{-/-}$ mice exhibit reduced levels of calcitonin mRNA transcripts in the thyroid. Furthermore, calcitonin treatment effectively suppressed the urinary DPD concentration in Glp-1r$^{-/-}$ mice. Taken together, these findings are consistent with an essential role for calcitonin in the regulation of bone turnover (31) and raise the possibility that modulation of GLP-1 receptor signaling may regulate bone resorption indirectly through the thyroid C cell.

In summary, our present findings demonstrate that genetic disruption of GLP-1 receptor signaling results in cortical osteopenia and bone fragility due to increased bone resorption by osteoclasts, in association with reduced thyroid calcitonin expression. Moreover, exogenous GLP-1 administration increased calcitonin expression in the thyroid glands of normal WT mice. These findings raise the possibility that clinical modulation of GLP-1 receptor signaling in human subjects, either through administration of GLP-1 receptor agonists or dipeptidyl peptidase-4 inhibitors, may indirectly regulate bone turnover in diabetic subjects. Given the recent observations of reduced bone density and increased fracture rates in diabetic subjects treated with thiazolidinediones (32, 33), more studies directed at understanding the actions of therapies that activate GLP-1 receptor signaling seem warranted.

Acknowledgments

We gratefully acknowledge Ms. Akemi Ito, Niigata Bone Science Institute, for the measurement of bone histomorphometry, and also Dr. H. Yamauchi, Japan Osteoporosis Foundation, for technical advice on calcitonin experiments.

Received September 19, 2007. Accepted November 9, 2007.

Address all correspondence and requests for reprints to: Yuichiro Yamada, M.D., Ph.D., Department of Internal Medicine, Division of Endocrinology, Diabetes, and Geriatric Medicine, Akita University School of Medicine, 1-1-1 Hondo, Akita City, Akita 010-8543, Japan. E-mail: yamada@gipc.akita-u.ac.jp.

This work was supported by Grants-in-Aid for Scientific Research from the Ministry of Education, Culture, Sports, Science, and Technology, Japan; by Health Sciences Research Grants for Comprehensive Research on Aging and Health from the Ministry of Health, Labor, and Welfare, Japan; and by an operating grant from the Juvenile Diabetes Research Foundation, Canada, to D.J.D.

Present address for K.T.: Anjo Kosei Hospital, Japan.

Disclosure Statement: The authors have nothing to disclose.

References

1. **Henriksen DB, Alexandersen P, Bjarnason NH, Vilsboll T, Hartmann B, Henriksen EE, Byrjalsen I, Krarup T, Holst JJ, Christiansen C** 2003 Role of gastrointestinal hormones in postprandial reduction of bone resorption. J Bone Miner Res 18:2180–2189
2. **Tsukiyama K, Yamada Y, Yamada C, Harada N, Kawasaki Y, Ogura M, Bessho K, Li M, Amizuka N, Sato M, Udagawa N, Takahashi N, Tanaka K, Oiso Y, Seino Y** 2006 Gastric inhibitory polypeptide as an endogenous factor

promoting new bone formation after food ingestion. Mol Endocrinol 20:1644–1651
3. **Bollag RJ, Zhong Q, Phillips P, Min L, Zhong L, Cameron R, Mulloy AL, Rasmussen H, Qin F, Ding KH, Isales CM** 2000 Osteoblast-derived cells express functional glucose-dependent insulinotropic peptide receptors. Endocrinology 141:1228–1235
4. **Zhong Q, Itokawa T, Sridhar S, Ding KH, Xie D, Kang B, Bollag WB, Bollag RJ, Hamrick M, Insogna K, Isales CM** 2007 Effects of glucose-dependent insulinotropic peptide on osteoclast function. Am J Physiol Endocrinol Metab 292:E543–E548
5. **Xie D, Cheng H, Hamrick M, Zhong Q, Ding KH, Correa D, Williams S, Mulloy A, Bollag W, Bollag RJ, Runner RR, McPherson JC, Insogna K, Isales CM** 2005 Glucose-dependent insulinotropic polypeptide receptor knockout mice have altered bone turnover. Bone 37:759–769
6. **Xie D, Zhong Q, Ding KH, Cheng H, Williams S, Correa D, Bollag WB, Bollag RJ, Insogna K, Troiano N, Coady C, Hamrick M, Isales CM** 2007 Glucose-dependent insulinotropic peptide-overexpressing transgenic mice have increased bone mass. Bone 40:1352–1360
7. **Henriksen DB, Alexandersen P, Byrjalsen I, Hartmann B, Bone HG, Christiansen C, Holst JJ** 2004 Reduction of nocturnal rise in bone resorption by subcutaneous GLP-2. Bone 34:140–147
8. **Henriksen DB, Alexandersen P, Hartmann B, Adrian CL, Byrjalsen I, Bone HG, Holst JJ, Christiansen C** 2007 Disassociation of bone resorption and formation by GLP-2: a 14-day study in healthy postmenopausal women. Bone 40:723–729
9. **Vilsboll T, Krarup T, Deacon CF, Madsbad S, Holst JJ** 2001 Reduced postprandial concentrations of intact biologically active glucagon-like peptide 1 in type 2 diabetic patients. Diabetes 50:609–613
10. **Crespel A, De Boisvilliers F, Gros L, Kervran A** 1996 Effects of glucagon and glucagon-like peptide-1-(7–36) amide on C cells from rat thyroid and medullary thyroid carcinoma CA-77 cell line. Endocrinology 137:3674–3680
11. **Lamari Y, Boissard C, Moukhtar MS, Jullienne A, Rosselin G, Garel JM** 1996 Expression of glucagon-like peptide 1 receptor in a murine C cell line: regulation of calcitonin gene by glucagon-like peptide 1. FEBS Lett 393:248–252
12. **Hansotia T, Baggio LL, Delmeire D, Hinke SA, Yamada Y, Tsukiyama K, Seino Y, Holst JJ, Schuit F, Drucker DJ** 2004 Double incretin receptor knockout (DIRKO) mice reveal an essential role for the enteroinsular axis in transducing the glucoregulatory actions of DPP-IV inhibitors. Diabetes 53:1326–1335
13. **Yamanouchi K, Yada E, Hozumi H, Ueno C, Nishihara M** 2004 Analyses of hind leg skeletons in human growth hormone transgenic rats. Exp Gerontol 39:1179–1188
14. **Parfitt AM, Drezner MK, Glorieux FH, Kanis JA, Malluche H, Meunier PJ, Ott SM, Recker RR** 1987 Bone histomorphometry: standardization of nomenclature, symbols, and units. Report of the ASBMR Histomorphometry Nomenclature Committee. J Bone Miner Res 2:595–610
15. **Udagawa N, Takahashi N, Yasuda H, Mizuno A, Itoh K, Ueno Y, Shinki T, Gillespie MT, Martin TJ, Higashio K, Suda T** 2000 Osteoprotegerin produced by osteoblasts is an important regulator in osteoclast development and function. Endocrinology 141:3478–3484
16. **Li X, Udagawa N, Itoh K, Suda K, Murase Y, Nishihara T, Suda T, Takahashi N** 2002 p38 MAPK-mediated signals are required for inducing osteoclast differentiation but not for osteoclast function. Endocrinology 143:3105–3113
17. **Schwartz AV** 2003 Diabetes mellitus: does it affect bone? Calcif Tissue Int 73:515–519
18. **Carnevale V, Romagnoli E, D'Erasmo E** 2004 Skeletal involvement in patients with diabetes mellitus. Diabetes Metab Res Rev 20:196–204
19. **Rakic V, Davis WA, Chubb SA, Islam FM, Prince RL, Davis TM** 2006 Bone mineral density and its determinants in diabetes: the Fremantle Diabetes Study. Diabetologia 49:863–871
20. **Bagi CM, Hanson N, Andresen C, Pero R, Lariviere R, Turner CH, Laib A** 2006 The use of micro-CT to evaluate cortical bone geometry and strength in nude rats: correlation with mechanical testing, pQCT and DXA. Bone 38:136–144
21. **Christensen J O, Svendsen OL** 1999 Bone mineral in pre- and postmenopausal women with insulin-dependent and non-insulin-dependent diabetes mellitus. Osteoporos Int 10:307–311
22. **Suzuki K, Sugimoto C, Takizawa M, Ishizuka S, Kikuyama M, Togawa H, Taguchi Y, Nosaka K, Seino Y, Ishida H** 2000 Correlations between bone mineral density and circulating bone metabolic markers in diabetic patients. Diabetes Res Clin Pract 48:185–191
23. **Majima T, Komatsu Y, Yamada T, Koike Y, Shigemoto M, Takagi C, Hatanaka I, Nakao K** 2005 Decreased bone mineral density at the distal radius, but not at the lumbar spine or the femoral neck, in Japanese type 2 diabetic patients. Osteoporos Int 16:907–913
24. **Suzuki K, Kurose T, Takizawa M, Maruyama M, Ushikawa K, Kikuyama M, Sugimoto C, Seino Y, Nagamatsu S, Ishida H** 2005 Osteoclastic function is accelerated in male patients with type 2 diabetes mellitus: the preventive role of osteoclastogenesis inhibitory factor/osteoprotegerin (OCIF/OPG) on the decrease of bone mineral density. Diabetes Res Clin Pract 68:117–125
25. **Wronski TJ, Yen CF, Burton KW, Mehta RC, Newman PS, Soltis EE, DeLuca PP** 1991 Skeletal effects of calcitonin in ovariectomized rats. Endocrinology 129:2246–2250
26. **Li M, Shen Y, Burton KW, DeLuca PP, Mehta RC, Baumann BD, Wronski TJ** 1996 A comparison of the skeletal effects of intermittent and continuous administration of calcitonin in ovariectomized rats. Bone 18:375–380
27. **Wallach S, Rousseau G, Martin L, Azria M** 1999 Effects of calcitonin on animal and in vitro models of skeletal metabolism. Bone 25:509–516
28. **Mochizuki K, Inoue T** 2000 Effect of salmon calcitonin on experimental osteoporosis induced by ovariectomy and low-calcium diet in the rat. J Bone Miner Metab 18:194–207
29. **Mosekilde L, Danielsen CC, Gasser J** 1994 The effect on vertebral bone mass and strength of long term treatment with antiresorptive agents (estrogen and calcitonin), human parathyroid hormone-(1–38), and combination therapy, assessed in aged ovariectomized rats. Endocrinology 134:2126–2134
30. **Giardino R, Fini M, Aldini NN, Gnudi S, Biagini G, Gandolfi MG, Mongiorgi R** 1996 Calcitonin and alendronate effects on bone quality in osteoporotic rats. J Bone Miner Res 21:S335 (Abstract)
31. **Huebner AK, Schinke T, Priemel M, Schilling S, Schilling AF, Emeson RB, Rueger JM, Amling M** 2006 Calcitonin deficiency in mice progressively results in high bone turnover. J Bone Miner Res 21:1924–1934
32. **Schwartz AV, Sellmeyer DE, Vittinghoff E, Palermo L, Lecka-Czernik B, Feingold KR, Strotmeyer ES, Resnick HE, Carbone L, Beamer BA, Park SW, Lane NE, Harris TB, Cummings SR** 2006 Thiazolidinedione use and bone loss in older diabetic adults. J Clin Endocrinol Metab 91:3349–3354
33. **Kahn SE, Haffner SM, Heise MA, Herman WH, Holman RR, Jones NP, Kravitz BG, Lachin JM, O'Neill MC, Zinman B, Viberti G** 2006 Glycemic durability of rosiglitazone, metformin, or glyburide monotherapy. N Engl J Med 355:2427–2443

Endocrinology **is published monthly by The Endocrine Society (http://www.endo-society.org), the foremost professional society serving the endocrine community.**

Available online at www.sciencedirect.com
ScienceDirect
Biochemical and Biophysical Research Communications 364 (2007) 175–180
BBRC
www.elsevier.com/locate/ybbrc

Genetic inactivation of GIP signaling reverses aging-associated insulin resistance through body composition changes

Chizumi Yamada [a], Yuichiro Yamada [a,b,*], Katsushi Tsukiyama [a,1], Kotaro Yamada [a], Shunsuke Yamane [a], Norio Harada [a], Kazumasa Miyawaki [c], Yutaka Seino [a,d], Nobuya Inagaki [a,e]

[a] *Department of Diabetes and Clinical Nutrition, Kyoto University Graduate School of Medicine, 54 Shogoin-Kawahara-cho, Sakyo-ku, Kyoto 606-8507, Japan*
[b] *Department of Internal Medicine, Division of Endocrinology, Diabetes and Geriatric Medicine, Akita University School of Medicine, Akita, Japan*
[c] *Department of Experimental Therapeutics, Translational Research Center, Kyoto University Hospital, Kyoto, Japan*
[d] *Kansai Electric Power Hospital, Osaka, Japan*
[e] *CREST of Japan Science and Technology Cooperation (JST), Kyoto, Japan*

Received 5 September 2007
Available online 9 October 2007

Abstract

Aging is associated with increased fat mass and decreased lean mass, which is strongly associated with the development of insulin resistance. Gastric inhibitory polypeptide (GIP) is known to promote efficient storage of ingested nutrients into adipose tissue; we examined aging-associated changes in body composition using 10-week-old and 50-week-old wild-type (WT) and GIP receptor knockout ($Gipr^{-/-}$) mice on a normal diet, which show no difference in body weight. We found that $Gipr^{-/-}$ mice showed significantly reduced fat mass without reduction of lean mass or food intake, while WT mice showed increased fat mass and decreased lean mass associated with aging. Moreover, aged $Gipr^{-/-}$ mice showed improved insulin sensitivity, which is associated with amelioration in glucose tolerance, higher plasma adiponectin levels, and increased spontaneous physical activity. We therefore conclude that genetic inactivation of GIP signaling can prevent the development of aging-associated insulin resistance through body composition changes.

Keywords: GIP; Body composition; Fat mass; Lean mass; Aging; Insulin resistance; Physical activity; GIP antagonism

Aging is associated with an increase in fat mass, thought to result from a sedentary lifestyle and *ad libitum* food intake over a prolonged period. Age-related accumulation of visceral fat is strongly associated with the development of insulin resistance [1–3]. On the other hand, reduction in skeletal muscle mass or sarcopenia also is a common feature of aging [4,5], increasing the risk for the development of insulin resistance [6]. To prevent the development of insulin resistance, various diet and exercise intervention trials have been conducted to favorably modify body composition by reducing fat mass while maintaining lean mass.

Gastric inhibitory polypeptide (GIP) is secreted from duodenal endocrine K cells in response to meal ingestion as an incretin, potentiating glucose-induced insulin secretion. Functional GIP receptors are expressed in adipose tissue [7] as well as in pancreatic β-cells, and GIP has been known to stimulate lipoprotein lipase activity and promote fatty acid incorporation into adipose tissue in the presence of insulin in cultured adipocytes [8–10]. Since GIP secretion is most strongly stimulated by fat ingestion [11,12], a high-fat diet is considered to be an ideal metabolic stress to induce hypersecretion of GIP for observation of

* Corresponding author. Address: Department of Internal Medicine, Division of Endocrinology, Diabetes and Geriatric Medicine, Akita University School of Medicine, Akita, Japan. Fax: +81 18 884 6117.
E-mail address: yamada@gipc.akita-u.ac.jp (Y. Yamada).
[1] Present address: Anjo Kosei Hospital, Japan.

0006-291X/$ - see front matter © 2007 Elsevier Inc. All rights reserved.
doi:10.1016/j.bbrc.2007.09.128

subsequent GIP action on adipocytes. The importance of GIP signaling on fat accumulation *in vivo* was first reported by Miyawaki et al. in mice with a targeted disruption of the GIP receptor gene ($Gipr^{-/-}$ mice), which exhibited reduced adiposity on a high-fat diet [9]. Since there was no difference in body weight between wild-type (WT) and $Gipr^{-/-}$ mice on a normal diet during a 50-week observation period [9], no attempt has been made to further investigate long-term GIP action in adipose tissue under normal nutritional conditions.

In the present study, we examined aging-associated changes in body composition using 10-week-old and 50-week-old WT and $Gipr^{-/-}$ mice on a normal diet. As in the previous study [9], the body weight of WT and $Gipr^{-/-}$ mice was almost identical, but computed tomography (CT) based-body composition analysis revealed that 50-week-old $Gipr^{-/-}$ mice had dramatically reduced fat mass and sustained lean mass compared with 50-week-old WT mice, which showed an age-related increase in fat mass and a decrease in lean mass.

Materials and methods

Animals. Generation of $Gipr^{-/-}$ mice was previously described [13]. Ten-week-old and 50-week-old male $Gipr^{-/-}$ mice and littermate WT controls on a C57BL/6 background were used. The animals had *ad libitum* access to standard rodent chow and water. Food intake (gram per mouse per day) was determined daily over 5 days in mice caged singly. All procedures were approved by the Animal Care Committee of Kyoto University Graduate School of Medicine.

CT-based body composition analysis. The mice were anesthetized with intraperitoneal injection of pentobarbital sodium (Dainippon Pharmaceutical, Japan) and their whole bodies were scanned along the body axis using the LaTheta (LCT-100M) experimental animal CT system (Aloka, Japan). Contiguous 1-mm slice images of the body including trunk and lower extremities were used for quantitative assessment using LaTheta software (version 1.00). Weights of total fat mass, which consists of visceral fat mass plus subcutaneous fat mass, and lean mass were determined and normalized by body weight.

Plasma hormone measurements. Plasma insulin, leptin, and adiponectin levels were determined by ELISA kits for mouse insulin (Shibayagi, Japan), mouse leptin (Morinaga, Japan), and mouse/rat adiponectin (Otsuka Pharmaceutical, Japan), respectively.

Insulin and glucose tolerance tests. For insulin tolerance test (ITT), 0.4 U/kg human insulin (Novonordisk, Denmark) was injected intraperitoneally after 5-h fasting. Oral glucose tolerance test (OGTT) was carried out following an overnight fast (16 h) and 2.0 g/kg glucose was loaded. Blood samples were taken at indicated times and blood glucose levels were measured by the enzyme-electrode method. HbA_{1c} was measured by immunoassay (DCA 2000 system, Bayer Diagnostics).

Insulin secretion from isolated islets. Isolation of pancreatic islets and batch incubation experiments were performed as described previously [14]. Briefly, 10 islets were collected in each tube and pre-incubated at 37 °C for 30 min in the medium containing 2.8 mM glucose, and incubated for another 30 min in the medium containing the indicated concentrations of glucose with 10^{-7} M human GIP or GLP-1 (Peptide Institute, Inc., Japan). Insulin secretion was measured by RIA using mouse insulin as a standard.

Telemetry recordings. Twelve- to 18-week-old WT and $Gipr^{-/-}$ mice weighing 27–30 g were used. The mice were anesthetized with pentobarbital sodium, and a small telemetric transmitter (TA10ETA-F20, Data Sciences Inc., USA) was implanted into the abdominal cavity. Seven to 14 days of recovery from the surgery was allowed before initiation of data collection. The mice were left undisturbed under a light/dark cycle of 14 h/10 h (lights on at 07:00 h and lights off at 21:00 h), and telemetry recordings for motor activity, body temperature (BT), and heart rate (HR) were performed every 2 min and averaged in 1-h bins using Dataquest A.R.T. software (version 2.1) (Data Sciences Inc.). The average for each bin from the same time point during a consecutive 5-day observation period was used for calculation.

Statistical analysis. Results are expressed as means ± SE. Statistical significance was assessed by ANOVA and unpaired Student's *t*-test, where appropriate. A P value of <0.05 was considered to be statistically significant.

Results

Aged $Gipr^{-/-}$ mice had reduced fat mass and sustained lean mass independent of changes in body weight or food intake

Body weight of WT and $Gipr^{-/-}$ mice was almost identical throughout the 50-week observation period (Fig. 1A). Body lengths measured at 10 and 50 weeks of age were also almost the same (data not shown). There was no difference in food intake between WT and $Gipr^{-/-}$ mice (Fig. 1B). CT-based analyses of body composition were performed as shown in Fig. 2A. There was no apparent difference in representative CT images showing abdominal fat (Fig. 2B, a) and thigh muscle (Fig. 2B, b) of 10-week-old WT and $Gipr^{-/-}$ mice. However, 50-week-old $Gipr^{-/-}$ mice had markedly less fat mass and a greater proportion of lean mass compared with 50-week-old WT mice (Fig. 2C). Total, subcutaneous, and visceral fat mass was similar in 10-week-old WT and $Gipr^{-/-}$ mice, but there

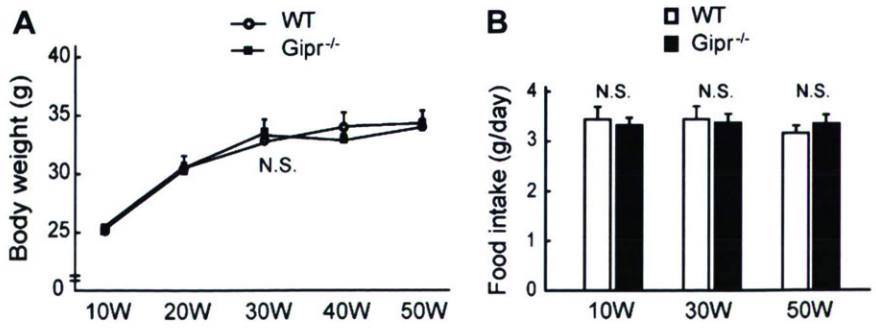

Fig. 1. Body weight and food intake. (A) Body weight of WT and $Gipr^{-/-}$ mice during the 50-week observation period. (B) Food intake (g/day) for each mouse was measured at 10, 30, and 50 weeks. $n = 6$–15 mice/group.

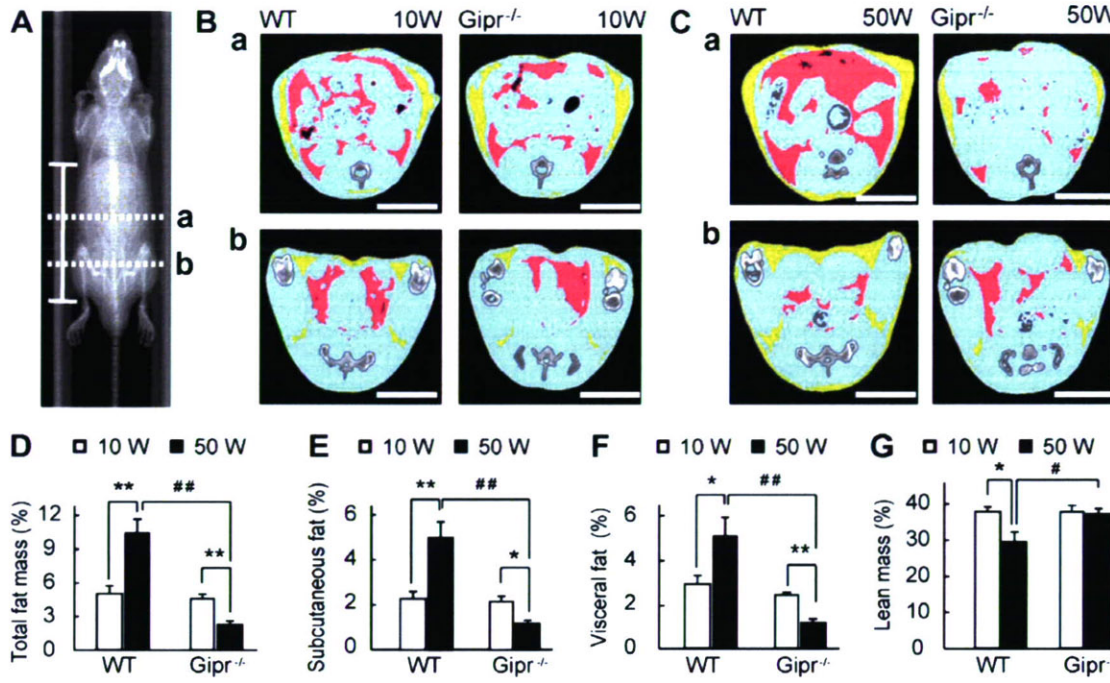

Fig. 2. CT-based body composition analyses. (A) The solid white bar indicates the observation area. Representative CT images showing abdominal fat (a) and thigh muscle (b) of 10-week-old (B) and 50-week-old (C) WT and Gipr$^{-/-}$ mice. The pink, yellow, and light blue areas represent visceral fat, subcutaneous fat, and lean mass, respectively. (D) Total fat mass, (E) subcutaneous fat mass, (F) visceral fat mass, and (G) lean mass, normalized to body weight, in 10-week-old and 50-week-old WT and Gipr$^{-/-}$ mice. $n = 6$–8 mice/group. $^{*}P < 0.05$; $^{**}P < 0.01$, 10-week-old vs 50-week-old mice, $^{\#}P < 0.05$; $^{\#\#}P < 0.01$, WT vs Gipr$^{-/-}$ mice. Scale bars, 1 cm. (For interpretation of the references to color in this figure legend, the reader is referred to the web version of this article.)

was a considerable difference in fat mass between 50-week-old WT and Gipr$^{-/-}$ mice (Fig. 2D–F). On the other hand, the weight of lean body mass was significantly increased in 50-week-old Gipr$^{-/-}$ mice (weights of lean body mass: 9.6 ± 0.5, 9.7 ± 0.6, 10.1 ± 0.7, and 12.4 ± 0.5 g for 10-week-old WT, 10-week-old Gipr$^{-/-}$, 50-week-old WT, and 50-week-old Gipr$^{-/-}$ mice, respectively, $P < 0.05$, 50-week-old WT vs Gipr$^{-/-}$ mice, $P < 0.01$, 10-week-old vs 50-week-old Gipr$^{-/-}$ mice). When normalized by body weight, lean mass was significantly decreased in 50-week-old WT mice, while 50-week-old Gipr$^{-/-}$ mice maintained the same percentage of lean mass as the young mice (Fig. 2G). There was no difference in organ weight between 50-week-old WT and Gipr$^{-/-}$ mice (liver weight: WT 1.64 ± 0.12 g vs Gipr$^{-/-}$ 1.63 ± 0.10 g, intestinal weight: WT 3.69 ± 0.21 g vs Gipr$^{-/-}$ 3.53 ± 0.40 g) as well as in 10-week-old WT and Gipr$^{-/-}$ mice (data not shown).

Aged Gipr$^{-/-}$ mice showed improved insulin sensitivity and amelioration in glucose tolerance

Insulin sensitivity was evaluated by ITT, and the glucose-lowering effect of insulin was decreased in 50-week-old WT mice compared with 10-week-old WT mice, indicating that WT mice had developed age-related insulin resistance (Fig. 3A). To the contrary, 50-week-old Gipr$^{-/-}$ mice were more insulin sensitive than 10-week-old Gipr$^{-/-}$ mice (Fig. 3B). There was no difference in glucose tolerance between 10-week-old and 50-week-old WT mice (Fig. 3C), but in 50-week-old WT mice, a compensatory increase in insulin secretion was required to achieve the same blood glucose levels as those in 10-week-old WT mice (Fig. 3E). In 50-week-old Gipr$^{-/-}$ mice, fasting and 15-min glucose levels were significantly decreased compared with 10-week-old Gipr$^{-/-}$ mice (76.4 ± 4.6 vs 56.0 ± 9.1 mg/dl at 0 min, $P < 0.01$, and 386.8 ± 20.6 vs 349.7 ± 46.0 mg/dl at 15 min, $P < 0.05$, for 10-week-old vs 50-week-old Gipr$^{-/-}$ mice, respectively), and the glycemic excursion between 30 min and 120 min was lower than that of 10-week-old Gipr$^{-/-}$ mice (Fig. 3D), although plasma insulin levels were not increased (Fig. 3F). Although Gipr$^{-/-}$ mice exhibited elevated post-challenge blood glucose levels, overall glycemic control as shown by HbA_{1c} was not worse in Gipr$^{-/-}$ mice compared with that in WT mice (3.10 ± 0.16, 2.84 ± 0.12, 2.80 ± 0.11, and $2.65 \pm 0.1\%$ for 10-week-old WT, 10-week-old Gipr$^{-/-}$, 50-week-old WT, and 50-week-old Gipr$^{-/-}$ mice, respectively). We also determined insulin secretion from isolated islets and found that the insulin secretory response to glucose and GLP-1 stimulation was intact in 10-week-old and 50-week-old Gipr$^{-/-}$ mice compared with their WT controls (Fig. S1(A) and S1(B)).

Aged Gipr$^{-/-}$ mice showed favorable changes in plasma adipocytokine levels and spontaneous hyperactivity

Consistent with fat mass, plasma leptin levels were significantly lower in 50-week-old Gipr$^{-/-}$ mice than in

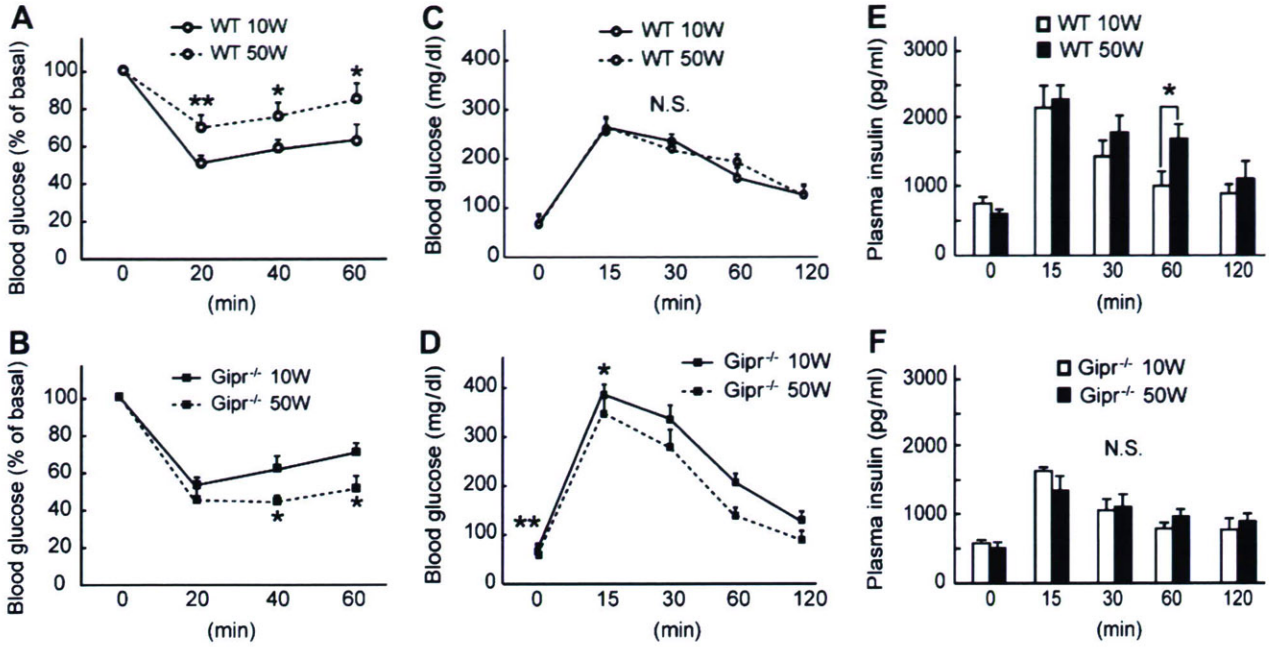

Fig. 3. Insulin and glucose tolerance tests. Results of insulin tolerance tests in 10-week-old and 50-week-old WT (A) and Gipr$^{-/-}$ (B) mice. $n = 6$–10 mice/group. Blood glucose levels during oral glucose tolerance test (OGTT) in 10-week-old and 50-week-old WT mice (C) and 10-week-old and 50-week-old Gipr$^{-/-}$ mice (D). Plasma insulin levels during OGTT (B) in 10-week-old and 50-week-old WT mice (E) and 10-week-old and 50-week-old Gipr$^{-/-}$ mice (F). $n = 5$–8 mice/group. $^{*}P < 0.05$; $^{**}P < 0.01$, 10-week-old vs 50-week-old mice.

50-week-old WT mice (Fig. 4A). On the other hand, plasma adiponectin levels were significantly higher in 50-week-old Gipr$^{-/-}$ mice than in 50-week-old WT mice (Fig. 4B). To investigate the underlying mechanism of increased lean mass, we used implanted telemetry chips to measure the 24-h profile of physical activity. WT and Gipr$^{-/-}$ mice both exhibited a robust rhythm of physical activity with intense activity during the dark phase and rest during the light phase (Fig. 4C). The average activity counts during a consecutive 5-day observation period showed that spontaneous activity was significantly increased in Gipr$^{-/-}$ mice both in light and dark phases

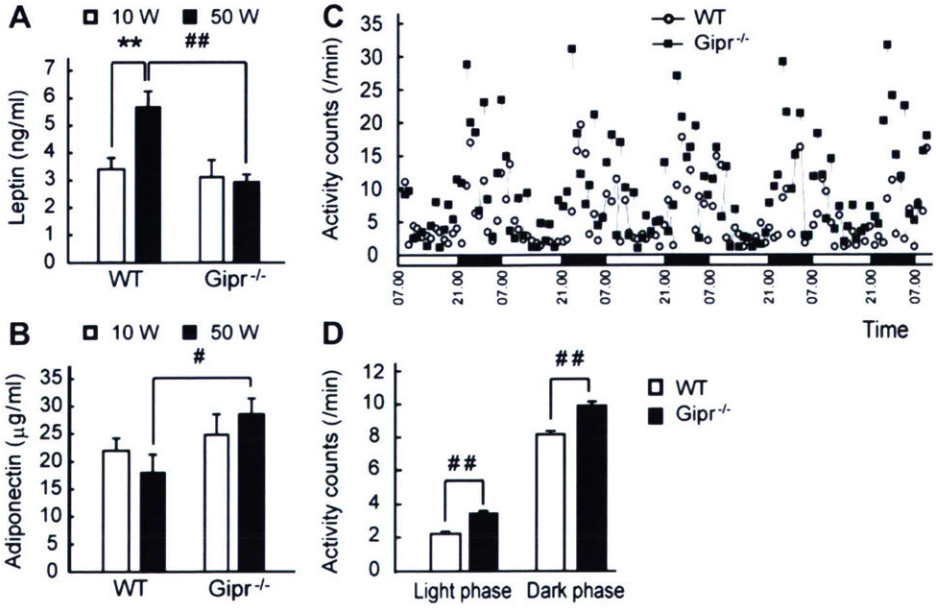

Fig. 4. Plasma adipocytokine levels and physical activity. (A) Plasma leptin and (B) adiponectin levels in 10-week-old and 50-week-old WT and Gipr$^{-/-}$ mice. $n = 6$–10 mice/group. (C) Representative circadian patterns of physical activity in a WT and Gipr$^{-/-}$ mouse under a 14 h/10 h light/dark cycle during a consecutive 5-day observation period. The white and black bar below the figure represents light phase and dark phase, respectively. (D) Average activity counts per minute in WT and Gipr$^{-/-}$ mice. $n = 5$ mice/group. $^{**}P < 0.01$, 10-week-old vs 50-week-old mice, $^{\#}P < 0.05$; $^{\#\#}P < 0.01$, WT vs Gipr$^{-/-}$ mice.

(Fig. 4D). However, BT in dark phase (Fig. S1(C) and S1(D)) and HR in both light and dark phases (Fig. S1(E) and S1(F)), measured simultaneously, were paradoxically decreased in Gipr$^{-/-}$ mice compared with WT mice despite increased physical activity.

Discussion

GIP was originally designated gastric inhibitory polypeptide for its influence on gastric acid secretion, and was later designated glucose-dependent insulinotropic polypeptide for its stimulation of insulin secretion from pancreatic β-cells. Studies using Gipr$^{-/-}$ mice have shown that GIP also has physiological roles in fat accumulation into adipose tissues [9] and calcium accumulation into bone [15], and thus a more appropriate referent of the acronym, gut-derived nutrient-intake polypeptide, has been recently proposed to more accurately reflect its physiological function [16]. The importance of inhibition of GIP signaling on fat accumulation *in vivo* was first demonstrated by Miyawaki et al., who found that male Gipr$^{-/-}$ mice fed a high-fat diet exhibit dramatically lesser adiposity than WT mice [9]. In addition, Hansotia et al. showed that single incretin (either GIP or glucagon-like peptide-1, GLP-1) receptor knockout mice as well as double incretin (both GIP and GLP-1) receptor knockout mice exhibited reduced body weight gain and adipose tissue accretion after a 20-week high-fat diet [17].

In the present study, we clearly show that 50-week-old Gipr$^{-/-}$ mice on a normal diet had reduced fat mass but sustained lean mass independent of changes in body weight or food intake, while 50-week-old WT mice showed dramatically increased fat mass and decreased lean mass, a characteristic of aging-associated changes in body composition. In young mice on normal diet, Xie et al. reported that the percentage of total fat was significantly increased and the amount of lean mass was reduced in 1-month-old and 5-month-old Gipr$^{-/-}$ females [18], however their results and our results are incommensurable because of the differences in sex, age, and breeding environments.

We also demonstrated that such alterations in body composition protected Gipr$^{-/-}$ mice from the development of insulin resistance (Fig. 3B). In C57BL/6 mice on a normal diet, glucose tolerance itself does not necessarily deteriorate with age because glucose-stimulated insulin secretion increases to compensate for age-related insulin resistance [19]. In our study, aged WT mice retained normal glucose tolerance, although a compensatory increase in insulin secretion was required to achieve the same blood glucose levels as in young mice. On the other hand, aged Gipr$^{-/-}$ mice showed better glucose tolerance during OGTT than in young Gipr$^{-/-}$ mice without incremental insulin secretion. Although Gipr$^{-/-}$ mice showed mild hyperglycemia compared with WT mice at early phases after oral glucose challenge, overall glycemic control as shown by HbA_{1c} was not worse in Gipr$^{-/-}$ mice. Moreover, the insulin secretory response to glucose and GLP-1 stimulation was intact in the islets of Gipr$^{-/-}$ mice compared with those of WT controls, indicating that β-cell function was not impaired by long-term inhibition of GIP signaling. We therefore conclude that aged Gipr$^{-/-}$ mice are protected from the development of aging-associated insulin resistance, which is associated with amelioration in glucose tolerance.

Stability of lean mass is another most important anti-aging phenomenon observed in aged Gipr$^{-/-}$ mice. Skeletal muscle accounts for more than half (~55%) of total lean mass, and maintenance of skeletal muscle mass is important for its metabolic quality as well as physical strength and functional status. There is an ongoing reduction of skeletal muscle mass in weight-stable elderly men and women [4,5], suggesting that weight stability in older individuals does not imply body composition stability, however, Gipr$^{-/-}$ mice gained lean mass with age, maintaining the same percentage of lean mass as the young mice (Fig. 2G). Favorable body composition with decreased fat mass and sustained lean mass can be promoted by physical exercise [20]. Our results clearly show that Gipr$^{-/-}$ mice are spontaneously hyperactive (Fig. 3C and D), which may contribute to favorable body composition and improved insulin sensitivity in older age. Surprisingly, BT and HR measured simultaneously were decreased in Gipr$^{-/-}$ mice compared with WT mice despite increased physical activity, characteristics resembling the physiological changes that take place in long-lived calorie restricted animals [21–23].

In conclusion, we have demonstrated that long-term inhibition of GIP signaling prevents development of aging-associated insulin resistance through body composition changes. Considering the difficulty of maintaining dietary restriction and exercise training for a prolonged period, GIP antagonism might be considered for further investigation as a therapeutic option against metabolic disorders related to aging.

Acknowledgments

This study was supported in part by Grants-in-Aid for Scientific Research from the Ministry of Education, Culture, Sports, Science and Technology, Japan, and by Health and Labour Sciences Research Grants from the Ministry of Health, Labour and Welfare, Japan.

Appendix A. Supplementary data

Supplementary data associated with this article can be found, in the online version, at doi:10.1016/j.bbrc.2007.09.128.

References

[1] P.J. Coon, E.M. Rogus, D. Drinkwater, D.C. Muller, A.P. Goldberg, Role of body fat distribution in the decline in insulin sensitivity and

glucose tolerance with age, J. Clin. Endocrinol. Metab. 75 (1992) 1125–1132.
[2] W.M. Kohrt, J.P. Kirwan, M.A. Staten, R.E. Bourey, D.S. King, J.O. Holloszy, Insulin resistance in aging is related to abdominal obesity, Diabetes 42 (1993) 273–281.
[3] S.B. Racette, E.M. Evans, E.P. Weiss, J.M. Hagberg, J.O. Holloszy, Abdominal adiposity is a stronger predictor of insulin resistance than fitness among 50–95 year olds, Diabetes Care 29 (2006) 673–678.
[4] D. Gallagher, E. Ruts, M. Visser, S. Heshka, R.N. Baumgartner, J. Wang, R.N. Pierson, F.X. Pi-Sunyer, S.B. Heymsfield, Weight stability masks sarcopenia in elderly men and women, Am. J. Physiol. Endocrinol. Metab. 279 (2000) E366–E375.
[5] V.A. Hughes, W.R. Frontera, R. Roubenoff, W.J. Evans, M.A. Singh, Longitudinal changes in body composition in older men and women: role of body weight change and physical activity, Am. J. Clin. Nutr. 76 (2002) 473–481.
[6] A.S. Ryan, Insulin resistance with aging: effects of diet and exercise, Sports Med. 30 (2000) 327–346.
[7] R.G. Yip, M.O. Boylan, T.J. Kieffer, M.M. Wolfe, Functional GIP receptors are present on adipocytes, Endocrinology 139 (1998) 4004–4007.
[8] B. Beck, J.P. Max, Gastric inhibitory polypeptide enhancement of the insulin effect on fatty acid incorporation into adipose tissue in the rat, Regul. Pept. 7 (1983) 3–8.
[9] K. Miyawaki, Y. Yamada, N. Ban, Y. Ihara, K. Tsukiyama, H. Zhou, S. Fujimoto, A. Oku, K. Tsuda, S. Toyokuni, H. Hiai, W. Mizunoya, T. Fushiki, J.J. Holst, M. Makino, A. Tashita, Y. Kobara, Y. Tsubamoto, T. Jinnouchi, T. Jomori, Y. Seino, Inhibition of gastric inhibitory polypeptide signaling prevents obesity, Nat. Med. 8 (2002) 738–742.
[10] S.J. Kim, C. Nian, C.H. McIntosh, Activation of lipoprotein lipase by glucose-dependent insulinotropic polypeptide in adipocytes. A role for a protein kinase B, LKB1, and AMP-activated protein kinase cascade, J. Biol. Chem. 282 (2007) 8557–8567.
[11] J.M. Falko, S.E. Crockett, S. Cataland, E.L. Mazzaferri, Gastric inhibitory polypeptide (GIP) stimulated by fat ingestion in man, J. Clin. Endocrinol. Metab. 41 (1975) 260–265.
[12] T. Krarup, J.J. Holst, K.L. Larsen, Responses and molecular heterogeneity of IR-GIP after intraduodenal glucose and fat, Am. J. Physiol. 249 (1985) E195–E200.
[13] K. Miyawaki, Y. Yamada, H. Yano, H. Niwa, N. Ban, Y. Ihara, A. Kubota, S. Fujimoto, M. Kajikawa, A. Kuroe, K. Tsuda, H. Hashimoto, T. Yamashita, T. Jomori, F. Tashiro, J. Miyazaki, Y. Seino, Glucose intolerance caused by a defect in the entero-insular axis: a study in gastric inhibitory polypeptide receptor knockout mice, Proc. Natl. Acad. Sci. USA 96 (1999) 14843–14847.
[14] C. Yamada, K. Nagashima, A. Takahashi, H. Ueno, Y. Kawasaki, Y. Yamada, Y. Seino, N. Inagaki, Gatifloxacin acutely stimulates insulin secretion and chronically suppresses insulin biosynthesis, Eur. J. Pharmacol. 553 (2006) 67–72.
[15] K. Tsukiyama, Y. Yamada, C. Yamada, N. Harada, Y. Kawasaki, M. Ogura, K. Bessho, M. Li, N. Amizuka, M. Sato, N. Udagawa, N. Takahashi, K. Tanaka, Y. Oiso, Y. Seino, Gastric inhibitory polypeptide as an endogenous factor promoting new bone formation after food ingestion, Mol. Endocrinol. 20 (2006) 1644–1651.
[16] Y. Yamada, K. Miyawaki, K. Tsukiyama, N. Harada, C. Yamada, Y. Seino, Pancreatic and extrapancreatic effects of gastric inhibitory polypeptide, Diabetes 55 (2006) S86–S91.
[17] T. Hansotia, A. Maida, G. Flock, Y. Yamada, K. Tsukiyama, Y. Seino, D.J. Drucker, Extrapancreatic incretin receptors modulate glucose homeostasis, body weight, and energy expenditure, J. Clin. Invest. 117 (2007) 143–152.
[18] D. Xie, H. Cheng, M. Hamrick, Q. Zhong, K.H. Ding, D. Correa, S. Williams, A. Mulloy, W. Bollag, R.J. Bollag, R.R. Runner, J.C. McPherson, K. Insogna, C.M. Isales, Glucose-dependent insulinotropic polypeptide receptor knockout mice have altered bone turnover, Bone 37 (2005) 759–769.
[19] E.H. Leiter, F. Premdas, D.E. Harrison, L.G. Lipson, Aging and glucose homeostasis in C57BL/6J male mice, FASEB J. 2 (1988) 2807–2811.
[20] P. Stiegler, A. Cunliffe, The role of diet and exercise for the maintenance of fat-free mass and resting metabolic rate during weight loss, Sports Med. 36 (2006) 239–262.
[21] L.K. Heilbronn, E. Ravussin, Calorie restriction and aging: review of the literature and implications for studies in humans, Am. J. Clin. Nutr. 78 (2003) 361–369.
[22] D. Chen, A.D. Steele, S. Lindquist, L. Guarente, Increase in activity during calorie restriction requires Sirt1, Science 310 (2005) 1641.
[23] M.P. Mattson, R. Wan, Beneficial effects of intermittent fasting and caloric restriction on the cardiovascular and cerebrovascular systems, J. Nutr. Biochem. 16 (2005) 129–137.

A real-time method of imaging glucose uptake in single, living mammalian cells

Katsuya Yamada[1], Mikako Saito[2], Hideaki Matsuoka[2] & Nobuya Inagaki[3]

[1]Department of Physiology, Hirosaki University School of Medicine, Aomori 036-8562, and CREST of Japan Science and Technology Agency, Honcho 4-1-8, Kawaguchi, Saitama 332-0012, Japan. [2]Department of Biotechnology and Life Science, Tokyo University of Agriculture and Technology, 2-24-16 Nakamachi, Koganei, Tokyo 184-8588, and CREST, Japan. [3]Department of Physiology, Akita University School of Medicine, 1-1-1 Hondo, Akita 010-8543, and Department of Diabetes and Clinical Nutrition, Kyoto University Graduate School of Medicine, Kyoto, and CREST, Japan. Correspondence should be addressed to N.I. (inagaki@metab.kuhp.kyoto-u.ac.jp) about cell assays and to H.M. (mhide@cc.tuat.ac.jp) about 2NBDG synthesis.

Published online 29 March 2007; doi:10.1038/nprot.2007.76

This protocol details a method for monitoring glucose uptake into single, living mammalian cells using a fluorescent glucose derivative, 2-[*N*-(7-nitrobenz-2-oxa-1,3-diazol-4-yl)amino]-2-deoxy-glucose (2-NBDG), as a tracer. The specifically designed chamber and superfusion system for evaluating 2-NBDG uptake into cells in real time can be combined with other fluorescent methods such as Ca^{2+} imaging and the subsequent immunofluorescent classification of cells exhibiting divergent 2-NBDG uptake. The whole protocol, including immunocytochemistry, can be completed within 2 d (except for cell culture). The procedue for 2-NBDG synthesis is also presented.

INTRODUCTION

Glucose is the major carbon source used in the cells of most organisms, so measurement of glucose uptake is an important research issue. In mammalian cells in particular, measuring glucose uptake of a heterogeneous population and/or differing activity status is of great interest[1,2]. To quantify glucose uptake, a variety of radiolabeled tracers such as [^{3}H] glucose[2], [^{14}C] 2-deoxy-D-glucose (2-DG)[3], [^{18}F] fluoro-2-deoxy-D-glucose[4] and [^{14}C] or [^{3}H] 3-O-methyl-D-glucose[5,6] have been used effectively. However, the spatial and temporal resolution of these methods is not high, and they cannot be used to visualize glucose uptake in single, living cells.

This protocol details a method for real-time monitoring of glucose uptake in single mammalian cells using a fluorescent D-glucose derivative, 2-[*N*-(7-nitrobenz-2-oxa-1,3-diazol-4-yl)amino]-2-deoxy-D-glucose (2-NBDG), as a tracer. 2-NBDG was initially developed for the rapid non-culture count of viable microbial cells and was successfully applied to *Escherichia coli*[7] and many other food-borne bacteria[8]. It has since been demonstrated in living mammalian cells that the uptake of 2-NBDG takes place through glucose transporters (GLUTs) in a concentration-, time- and temperature-dependent manner[9]. A short-period application of 2-NBDG produced a remarkable increase in the fluorescence intensity in COS-1 cells over-expressing GLUT2, whereas the increase was barely detectable in mock-transfected cells[9]. In mouse insulin-secreting clonal MIN6 cells[10], uptake was inhibited by cytochalasin B, a specific blocker for GLUTs, and by D-glucose in a dose-dependent manner[9]. Kinetic analysis using fluorometry further revealed that the time course of the uptake into MIN6 cells was almost linear up to 2 min, and apparent K_m values calculated from the Eadie–Hofstee transformation using the initial velocity of uptake at 1 min were similar to those reported for D-glucose and the non-metabolizable glucose analog, 3-O-methyl-D-glucose, found in pancreatic islets and cultured β-cells[9].

In recent years, 2-NBDG has been shown to be useful for monitoring glucose uptake into a variety of mammalian cells. These include pig vascular smooth muscle cells[11], rabbit enterocytes[12], rat cardiomyocytes[13], rat and mouse astrocytes and neurons in culture and *in vivo*[14–18], human and murine tumor cell lines[19,20] and adipocyte cell lines[21]. Inhibition of 2-NBDG uptake by D-glucose has been confirmed using vascular smooth muscle cells[11] and tumor cell lines[20], and inhibition by cytochalasin B in rat astrocytes[15].

Direct visualization of glucose uptake without using isotopes makes the 2-NBDG method quite attractive[13,21,22]. In addition, 2-NBDG has recently been used to investigate cell type–specific uptake of glucose and intercellular communication, such as that in the CNS[14–16,18]. Simple superfusion of 2-NBDG over cells using a flow-through system allows simultaneous monitoring of differing glucose uptake into heterogeneous cells. However, care should be taken because fluorescence intensity is an arbitrary measure. Thus, quantification requires stability of the system as well as accurate procedures. Accordingly, we focus here on the construction of a flow-through system as well as a practical protocol for measurement of 2-NBDG uptake. Also presented are procedures for combining this method with Ca^{2+} imaging by fura-2 and subsequent immunocytochemical identification of cells[9].

The limitation in the use of 2-NBDG is related to its intracellular fate. We previously found that 2-NBDG is metabolized to a phosphorylated fluorescent derivative at the C-6 position (2-NBDG 6-phosphate) after entering into *E. coli* cells and then decomposes to a non-fluorescent derivative[23]. Thus, the fluorescence intensity should reflect a dynamic equilibrium of generation and decomposition of 2-NBDG and the fluorescent metabolite. The use of 2-NBDG in the study of intracellular glucose metabolism is thus limited, and experiments must be carefully performed.

The protocols for 2-NBDG synthesis are described as well as the detailed characteristics of 2-NBDG, for researchers who may want to use a large amount of purified 2-NBDG.

MATERIALS

REAGENTS

- DMEM containing 4,500 mg l^{-1} D-glucose (DMEM-HG) (Life Technologies, cat. no. 12800-082)
- MIN6 cells (see REAGENT SETUP)
- Ca^{2+}, Mg^{2+}-free (CMF) PBS (see REAGENT SETUP)
- Trypsin–EDTA (Life Technologies, cat. no. 25200-023)
- 2-NBDG (see **Box 1** and **Fig. 1**)
- Krebs Ringer bicarbonate buffer (KRB) (see REAGENT SETUP)

BOX 1 | SYNTHESIS OF 2-[*N*-(7-NITROBENZ-2-OXA-1,3-DIAZOL-4-YL)AMINO]-2-DEOXY-D-GLUCOSE (2-NBDG)

REAGENTS

- D-glucosamine (Sigma)
- $NaHCO_3$ (Kokusan Chemical)
- *N*-(7-nitrobenz-2-oxa-1,3-diazol-4yl-)amino chloride (NBD-Cl; Wako)
- Sephadex A-50 (Amersham Pharmacia)
- Sephadex LH-20 (Amersham Pharmacia)
- D_2O (100 atom %D; Aldrich)
- Acetonitrile (chromato-grade for thin-layer chromatography (TLC); Kokusan Chemical)
- Triethanolamine (TEA; Kokusan Chemical)
- TLC plate silica gel 60 F_{254} (Merck Japan Limited)

EQUIPMENT

- Rotary evaporator (N-1000; EYELA)
- Freeze-dryer (FD-1; EYELA)
- DEAE (2-(diethylamino)ethyl-) Sephadex A-50 column and Sephadex LH-20 column (see REAGENT SETUP below)

REAGENT SETUP

DEAE Sephadex A-50 column and Sephadex LH-20 column Equilibrate DEAE Sephadex A-50 and Sephadex LH-20 with dH_2O, and fill into respective glass columns according to the standard protocols recommended by the company. The resin volume is 30× 200 mm^2 (diameter times length) for DEAE Sephadex A-50 and 20× 250 mm^2 (diameter times length) for Sephadex LH-20. Operate both columns according to the standard protocol of gel filtration.

PROCEDURE

1. Dissolve 0.5 g D-glucosamine in 10 ml 0.3 M $NaHCO_3$ solution in a 100-ml Erlenmeyer flask (solution A), and dissolve 0.5 g NBD-Cl in 20 ml methanol in a 50-ml beaker (solution B).
2. Mix solutions A (10 ml) and B (20 ml) in a 100-ml recovery flask (egg plant flask). Send N_2 gas into the flask to purge the inside air and finally seal the flask with a silicon rubber cork with a balloon filled with N_2 gas. Wrap the flask with aluminum foil to shield from light. Shake the flask in a water bath shaker at 30 °C for 18 h.
3. Remove precipitates in the reaction mixture by filtration through a nylon mesh (10 μm) (or glass wool) using an aspirator. Collect the filtrate in another recovery flask.
4. Evaporate the reaction mixture to remove the solvent. A slight amount of solvent remaining does not matter.
5. Add 10 ml dH_2O to the flask to dissolve the product (solution C).
6. Load solution C on the Sephadex A-50 column after filtration through a filter paper. Elute the column with dH_2O and collect yellow and orange fractions together. It is advisable to collect small fractions and then combine them after TLC (Step 7).
7. Frequently analyze the elute by TLC around the beginning and the end of the elution of yellow and orange components. This is done by performing these steps: (i) Spot 100-μl aliquots on the silica gel plate and develop with a solvent composed of $CH_3CN:H_2O$ = 17:3 (v/v). (ii) Detect fluorescent spots under a UV illuminator. (iii) Heat the plate to visualize sugar spots. (iv) Determine the retention factors (R_f) of fluorescent spots and sugar spots. A typical result is shown in **Figure 1a**. R_f of 2NBDG is 0.68.

Note: Maximize the 2NBDG yield but minimize the collection volume to be treated in the next step. Typically, the collection volume is approximately 200 ml (solution D).

8. Reduce the volume of solution D to about 5 ml by evaporation. Observe the solution volume carefully and stop evaporation before the volume becomes too small (this is solution E).
9. Load solution E on the Sephadex LH-20 column. Elute the column with dH_2O. Yellow, orange and brown fractions follow in that order. Collect the orange fractions.
10. Frequently analyze the eluate by HPLC around the beginning and the end of elution of the orange component. This is done by following these steps: (i) Inject 2–5-μl aliquots into the sample injection port and elute with solvent composed of $CH_3CN:H_2O$ = 17:3 (v/v). (ii) Adjust the elution speed to 0.5 ml min^{-1} and monitor the optical density of the eluate at 475 nm. A typical result is shown in **Figure 1b**. The peaks at 10.5 min (P_1) and 11.8 min (P_2) represent the β-D-anomer and α-D-anomer of 2-[*N*-(7-nitrobenz-2-oxa-1,3-diazol-4-yl)amino]-2-deoxyD-glucose (2-NBDG), respectively. (iii) Estimate the purity using the formula (P_1 area + P_2 area)/(All peaks) × 100%.

Note: This is done to find the optimal condition to collect a maximum amount of 2-NBDG with highest purity. Successful gel filtration gives more than 98% purity.

11. Collect fractions containing 2-NBDG of more than 98% purity (solution F). Expected volume is 5 ml per fraction× 15–20 fractions.

Note: In case of low purity, repeat gel filtration using a fresh Sephadex LH-20 column.

12. Reduce the volume of solution F to approximately 10 ml by evaporation (solution G).
13. Freeze solution G in liquid N_2 to lyophilize the product. A yield of approximately 100 mg is expected.

Note: Dissolve the dry matter with dH_2O and store at 4 °C and use within 4 weeks. Keep the dry matter at −20 °C for longer storage.

14. Confirm the identity of the product by proton nuclear magnetic resonance analysis (^{1}H-NMR). Dissolve the dry matter of the product with deuterium oxide and immediately analyze it using ^{1}H-NMR under 500 MHz. A typical result is shown in **Figure 1c**. Assign peaks to respective protons of pyranose and NBD.

BOX 1 | CONTINUED

15. Analyze the mass spectrum by fast atom bombardment mass spectrometry (FAB-MS) (m/z) using triethanolamine as the matrix. Confirm the peak at 343 that corresponds to 2-NBDG-H^+.

16. Analyze the fluorescent spectrum according to the following steps: (i) Dissolve 2-NBDG with distilled water to adjust the concentration to 10 μg ml^{-1}. (ii) Measure emission spectrum from 495 to 650 nm under excitation at 475 nm. (iii) Measure the fluorescence intensity at 550 nm by scanning the excitation wavelength from 300 to 520 nm. (iv) Typical spectra depicted in **Figure 1d** will be obtained.

- D-Glucose (Wako)
- Cytochalasin B (Sigma, cat. no. C6762)

EQUIPMENT

- 35-mm culture dish with an oval glass bottom (14 × 5 mm^2, 0.08–0.12-mm-thick glass) (Matsunami Glass Ind., Osaka, Japan, cat. no. D110500) **Fig. 2**) (see EQUIPMENT SETUP)
- Cover glass (cut into 10 × 11 mm^2 pieces) (Corning, cat. no. 1)
- Vacuum grease (HVAC-G; Shin-Etsu Silicone, Tokyo, Japan)
- Round-type, heating glass stage with a flat surface (0.5 mm thick, MPF-10HF) (Kitazato Supply, Fuji, Shizuoka, Japan) or equivalent
- Superfusate warmer (MT-1, dead volume= 0.13 ml; Narishige, Tokyo; or SF-28, Warner)
- Thermistor probe (IT-23, diameter= 0.23 mm; World Precision Instruments)
- Digital thermometer (TH-5; Physitemp Instruments, Clifton, NJ)
- Inverted microscope (Nikon DIAPHOT TMD300 or equivalent) equipped with long working distance (WD) objective lenses: Nikon CF Plan×2 (NA 0.05, WD 5.8 mm), Plan ×4 DL (NA 0.13, WD 16.2 mm), Plan ×10 DL (NA 0.3, WD 9.2 mm) and Plan Fluor ×20 DLL Ph2 (NA 0.5, WD 2.1 mm) or Plan ELWD ×20 DL Ph2 (NA 0.4, WD 7.0–8.1 mm)
- Dichroic mirror (DM), excitation (Ex) and barrier (BA) filters used for 2-NBDG measurement are Nikon DM 505, Ex 480/40 and BA520–560, respectively
- Neutral density (ND) filters: Nikon ND2 (50%), ND4 (25%) and ND8 (12.5%) for fluorescent imaging; ND2 and ND16 (6.25%) for transmitted light imaging; variable intensity is obtained by using these filters in combination
- Peristaltic pump (MCP Standard pump equipped with 12 roller-pumphead MS/CA4-12; Ismatec SA, Glattbrugg, Switzerland)
- Vacuum pump (DAP-15; Alvac, Kanagawa, Japan)
- Vacuum pressure gauge
- Imaging system (Argus 50; Hamamatsu Photonics, Hamamatsu, Japan) or equivalent
- Silicon intensified target (SIT) camera (Hamamatsu Photonics) or equivalent

REAGENT SETUP

CMF-PBS NaCl, 137 g l^{-1}; KCl, 4.0 g l^{-1}; $NaH_2PO_42H_2O$, 0.36 g l^{-1}; KH_2PO_4, 0.18 g l^{-1}; $NaHCO_3$, 12 g l^{-1}; glucose, 11 g l^{-1}; pH 7.30–7.35.

KRB NaCl, 129 mM; KCl, 4.7 mM; KH_2PO_4, 1.2 mM; $CaCl_2$, 1.0 mM; $MgSO_4$, 1.2 mM; $NaHCO_3$, 5.0 mM; HEPES, 10 mM; pH 7.35–7.40.

Preparation of MIN6 cells (i) Prepare a total of 92 ml DMEM-HG containing 13% FBS (FBS-DMEM-HG) in two 50-ml tubes by adding 6 ml FBS to 40 ml DMEM-HG for each tube. (ii) Prepare two 10-cm culture dishes and add 10 ml FBS-DMEM-HG into each dish. (iii) Prepare 15 ml CMF-PBS. (iv) Prepare 1 ml trypsin–EDTA. (v) Warm (i–iv) at 37 °C for the following steps. (vi) Exchange medium in a 10-cm dish culturing MIN6 cells with 10 ml CMF-PBS. (vii) Suck CMF-PBS with a vacuum pump and add 5 ml CMF-PBS and 1 ml 0.25% trypsin–EDTA. (viii) After waiting for 1–2 min, peel off the cells gently by sucking and blowing the medium through a 10-ml pipette. (ix) Suck the cell suspension (approximately 6 ml) and transfer into 30 ml FBS-DMEM-HG. (x) Centrifuge at 1,500 r.p.m. for 3 min (in a Kubota 5200, Kubota Co., Tokyo, Japan). (xi) Suck the supernatant and add 10 ml FBS-DMEM-HG. (xii) Triturate five times with a 10-ml pipette (let cells go back and forth gently within the pipette using a Pipette aid). (xiii) Centrifuge at 1,500 r.p.m. for 1 min (in a Kubota 5200, Kubota Co., Tokyo, Japan). (xiv) Add 3 ml FBS-DMEM-HG. (xv) Triturate 40 times with a 5-ml pipette, and count cells within 30 s. (xvi) Dilute cell suspension at 20 × 10^4 ml^{-1}. (xvii) For passage, transfer 0.5 ml cell suspension into each of the 10-cm dishes containing 10 ml FBS-DMEM-HG (ii). (xviii) For the experiment, triturate 20 times again and transfer cell suspension (145 μl) onto the glass part of a glass-bottom culture dish. Moisten the glass part of the dish with 100 μl FBS-DMEM-HG beforehand and suck medium just before plating. (xix) Observe cells after waiting for 5 min and readjust the dilution ratio so that most cells are seen separately. If too many cells are observed, blow off cells with yellow tip and dilute again. (xx) Leave the cells in a CO_2 incubator (5% CO_2, 37 °C) for 30 min until the cells adhere to the glass. (xxi) Add 2 ml FBS-DMEM-HG to fill the whole culture dish. (xxii) Perform measurement of 2-NBDG uptake before many clusters of MIN6 cells are formed. To assess the health of MIN6 cells during the course of the passages, check [Ca^{2+}] responsiveness to glucose stimulation similarly to the procedure described in **Box 2** (**Figs. 2** and **3**).

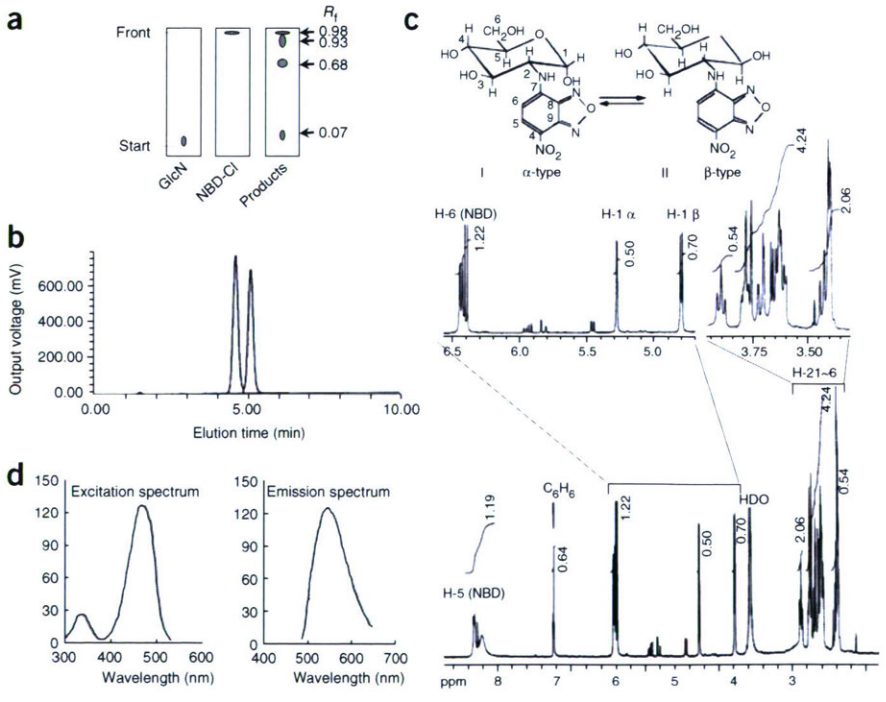

Figure 1 | Analytical data of 2-[*N*-(7-nitrobenz-2-oxa-1,3-diazol-4-yl)amino]-2-deoxyD-glucose (2-NBDG). (**a**) TLC. Silica gel plate, solvent $CH_3CN:H_2O$ = 17:3, R_f (fluorescent spots: 2NBDG = 0.68, NBD-Cl = 0.98, GlcN = 0.07, unidentified by-products = 0.93). (**b**) HPLC spectrum. Column: TSKgel amide-80, eluent: $CH_3CN:H_2O$ = 17:3, flow rate: 1.0 ml min^{-1}, detection: $OD_{475\,nm}$. Two peaks: α-D-anomer and β-D-anomer. (**c**) ^{1}H-NMR spectrum. 500 MHz in D_2O, δ4.78 p.p.m. (d, $J_{1,2}$ = 10 c.p.s., axial–axial, β), δ5.27 p.p.m. (d, $J_{1,2}$ = 4 c.p.s., axial–equatorial, α), δ3.4–3.95 p.p.m. (m, H-2–H-6), δ6.4 p.p.m. (*m*, H-6 NBD), δ8.2–8.35 p.p.m. (*m*, H-5 NBD). (**d**) Fluorescence spectra. Emission spectrum: λ_{EM} = 495–650 nm, λ_{EX} = 475 nm; excitation spectrum: λ_{EM} = 550 nm, λ_{EX} = 300–520 nm.

Preparation of 2-NBDG solution Dissolve 2-NBDG in KRB (pH 7.35–7.40). The concentration of 2-NBDG and glucose should be determined according to the purpose of the experiment (see PROCEDURE). ▲ CRITICAL Do not freeze the 2-NBDG solution, as it will precipitate when thawing.

EQUIPMENT SETUP

Culture dish and superfusion chamber Mark random scratches beforehand on the outside of the oval glass bottom of the culture dish with a diamond knife for later immunocytochemical identification of the cells. Although a round glass-bottom culture dish can be used, the medium flow is smoother in an oval one. Prepare a plastic plate with a leaf-shaped hole, as the glass part of the dish is too shallow to obtain a stable medium flow (**Fig. 2**). This plate can be readily made using the culture dish by removing its glass bottom. Attach the plate tightly to the plastic part of the culture dish with vacuum grease just before experiment (see PROCEDURE). Thus, the depth of the glass part of the dish is doubled. A silicone rubber plate with an oval hole can be used instead of the plastic plate (**Fig. 2**). In this case, small projection portions made on the silicone plate (slashed part in **Fig. 2**) will help precise positioning of the cover glass.

Attach a square small cover glass (10× 11 mm^2) to the plastic plate with a small amount of vacuum grease to cover the central part of the oval glass bottom (**Fig. 2**). The cover glass helps to smooth flow while decreasing the volume of superfusate, assuring rapid change of the solution, and also helps to prevent optical noise owing to fluctuation of the medium surface level. When only the central part of the bath is covered, drugs can be directly dropped onto the small gap upstream of the cover glass. In addition, local temperature at the region of interest below the cover glass can be easily checked during the experiment. ▲ CRITICAL Adjust the position, angle and height of the inlet and, especially, the outlet needle carefully **Fig. 2**) to obtain smooth laminar flow.

Place a round, flat-surface heating glass stage on the microscope stage. A plastic holder plate (14 × 14 × 0.9 cm^3) with an opening (approximately 35 mm) in the central part should be fixed on the heating stage. The inner diameter of the opening must be determined by the outer diameter (sometimes tapered) of the dish used. Mount the culture dish into the plastic holder plate so that the glass bottom of the culture dish directly touches the heating glass stage (37 °C). Long-WD objective lenses (see EQUIPMENT) are required owing to the thickness of the heating glass stage.

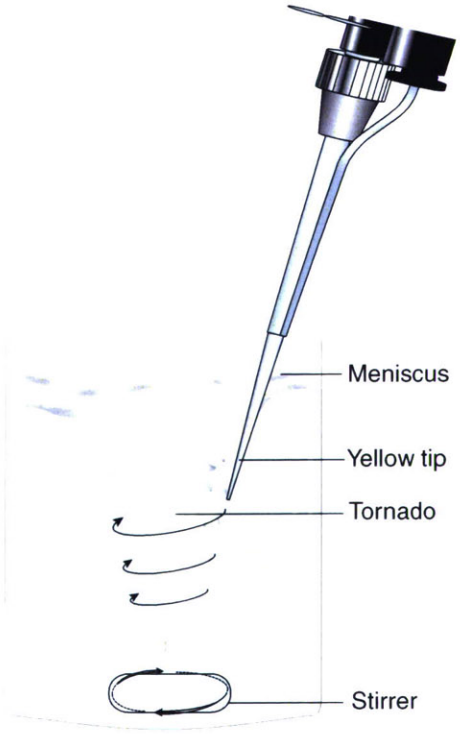

Figure 3 | Dissolving fura-2/AM in DMSO into Krebs Ringer bicarbonate buffer (KRB).

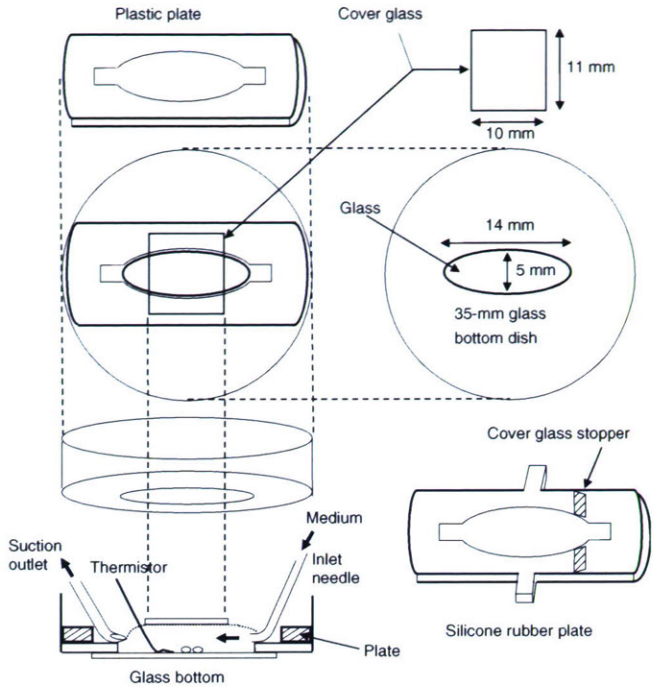

Figure 2 | A culture dish–based chamber for live-cell imaging. A plastic (or silicone rubber) plate is attached to the glass-bottom culture dish to make a bath for superfusion. The central part of the bath is covered by a cover glass to promote smooth flow and rapid exchange of superfusate.

Check the temperature of the superfusate at the region of interest by inserting a very thin thermistor probe between the cover glass and the glass bottom before (or sometimes during) the experiment. An extra dish with no cells should be prepared for just this purpose. Constant temperature at the area of interest (36.5–37.5 °C) indicates that the whole chamber system is working properly.

Use a low-pulsation peristaltic pump and a vacuum pump for the delivery and the removal of the superfusate, respectively. Substitution of the polyethylene tube with a stainless steel pipe of very thin internal diameter helps to decrease dead volume from the superfusate bottle to the dish. Adjust the vacuum pressure with a screw valve and/or three-way valves at 30–40 kPa so that cells are left on the dish. A simple delivery system using hydrostatic pressure can be used instead of a peristaltic pump. ▲ CRITICAL The shape of the end of the outlet needle for removing superfusate is critical to achieving a stable flow. The main consideration is that the hole at the end should be opened in the upward direction (**Fig. 2**). Bend a stainless steel needle (20G, 0.90 × 70 mm) smoothly so as not to interfere with smooth medium flow inside the needle. Then enlarge the hole at the end of the needle obliquely to the axis as large as is possible using sandpaper so that the needle has an elongated hole on the very tip. When the position and the angle of the needle are adequate, superfusate is sucked constantly from the hole together with air, making a constant sucking sound. We have designed a height-, angle- and rotation-adjustable small holder for the needle for this purpose (**Fig. 4**); this is available from Narishige Scientific Instruments, Tokyo, Japan (see **Table 1**).

PROCEDURE

Preparation for superfusion ● TIMING 5 min

1| Take the culture dish out from the CO_2 incubator, and gently absorb the culture medium outside the glass bottom part of the dish. Then wipe the medium left on the plastic floor of the dish completely using a cotton swab, leaving medium only on the glass bottom part.

2| Attach the plastic plate with a leaf-shaped hole (**Fig. 2**) tightly to the culture dish with silicone vacuum grease.

BOX 2 | $[Ca^{2+}]_I$ MEASUREMENT COMBINED WITH MEASUREMENT OF 2-[N-(7-NITROBENZ-2-OXA-1,3-DIAZOL-4-YL)AMINO]-2-DEOXY-D-GLUCOSE (2-NBDG) UPTAKE IN PANCREATIC ISLET CELLS

REAGENTS

- Fura-2/AM (Dojindo, cat. no. 343-05401)
- DMSO (Dojindo)
- Ca^{2+}-free Krebs Ringer bicarbonate buffer (KRB) (see REAGENT SETUP below)
- $CaCl_2$ (0.1 M solution) (Wako)
- Glucose (Wako)
- Eagle's minimum essential medium containing kanamycin (60μg ml^{-1}) (Nissui, cat. no. 1) and 5.6 mM glucose (MEM)
- EGTA (0.1 M solution) (Sigma, cat. no. E-4378)
- BSA (Fraction V, pH of 1% aqueous solution is 5.2) (Sigma, cat. no. A-4503)
- Tolbutamide (Sigma, cat. no. T0891)
- Guinea pig anti-swine insulin antibody (Dako, cat. no. N1542)
- Rabbit anti-porcine glucagon antibody (Dako, cat. no. L1813)
- Rhodamine-conjugated goat anti-rabbit IgG (Cappel)
- Rhodamine-conjugated goat anti–guinea pig IgG (Chemicon)
- Sodium phosphate buffer (PB)
- Paraformaldehyde (Nakalai)

EQUIPMENT

- Non-coated glass-bottom dishes
- Dichroic mirror and barrier filter (Nikon DM400) (BA510 LP)
- Excitation filter Hamamatsu MC340- and 380-nm excitation filters

REAGENT SETUP

Preparation of islet cells (i) Isolate islets of Langerhans from 8–12-week-old Harlan Sprague–Dawley rats by collagenase digestion under nembutal anesthesia[25]. (ii) Transfer the islets into ice-cold Ca^{2+}-free KRB containing 5.6 mM glucose. (iii) Centrifuge at 800 r.p.m. for 30–60 s (in a himac CR5B from Hitachi High Technologies, Tokyo, Japan) at room temperature (22–28°C) and wash sediments with KRB containing 0.1 mM Ca^{2+}, 0.1% BSA and 5.6 mM glucose (repeat three times). A small addition of Ca^{2+} at this point will mitigate cellular damage by EGTA treatment in the next stage. (iv) Dissociate the islet into single cells by incubation for 15–17 min at room temperature in 200μl Ca^{2+}-free KRB containing 1 mM EGTA, 0.1% BSA and 5.6 mM glucose. Make a 0.1 M EGTA stock solution for this purpose (adjust pH to 7.4 by 1 N HCl). (v) Triturate 8–12 times using a yellow tip. (vi) Transfer the dissociated islets into 10 ml of MEM supplemented with 10% FBS (MEM-FK). (vii) Centrifuge at 800 r.p.m. for 3 min (in a himac CR5B from Hitachi High Technologies, Tokyo, Japan) at room temperature, discard the supernatant by suction pipette and re-suspend the cells in 200μl of MEM-FK. (viii) Plate a small amount of single cells (such as 30μl) on a culture dish in the center of the oval glass bottom (**Fig. 2**). (ix) Leave the cells in a CO_2 incubator (5% CO_2, 37 °C) for 20 min until cells adhere to the glass bottom. (x) Add 0.5–1.0 ml of culture medium slowly. Cells can be maintained in the CO_2 incubator for up to 2 d. However, Ca^{2+} responsiveness to glucose stimulation is obtained from a maximal number of healthy β-cells during the several hours after plating.

Ca^{2+}-free KRB (mM) NaCl, 129; KCl, 4.7; KH_2PO_4, 1.2; $MgSO_4$, 1.2; $NaHCO_3$, 5.0; HEPES, 10; pH 7.35.

Preparation of fura-2/AM solution

1. Dissolve 10 μl 1 mM fura-2/AM in DMSO solution into 10 ml KRB containing 2.8 mM glucose and 1 mM Ca^{2+} (final concentration of fura-2/AM, 1 μM), as described.

Note: Use DMSO that has been kept dried, since moisture absorption interferes with dissolution of fura-2/AM (in DMSO) into aqueous solution. Detergents to promote dissolution such as Cremophor EL (C5135, Sigma) are not necessary. The volume of fura-2/AM-containing KRB should be determined according to the chamber volume and the total dead volume in the inlet tubing.

2. Stir vigorously 10 ml KRB solution in a small glass vial (such as 12.5 ml) using a very small stirrer magnet so that a stable, tornado-like vortex appears in the central part of the solution (**Fig. 3**). Use a high-performance magnetic stirrer.

Note: If a low-performance stirrer is used, the position of the vortex may move right or left unstably, and dissolution will be unsuccessful.

3. Push out the fura-2/DMSO solution continuously and as slowly as possible from a yellow tip. Hold the tip almost perpendicularly along, but slightly outside, the vortex wall. When dissolution is successful, fura-2/AM in DMSO disappears spirally into the KRB solution similar to a pale smoke or is almost unseen. Never suck the KRB into the tip by releasing pushing force.

Note: If water leaks into the tip, small oil droplets will be seen coming out from the tip into the KRB when fura-2/AM is pushed out, and the tip end will be polluted by white deposit. These droplets are due to undissolved fura-2, indicating unsuccessful dissolution. Discard the tip and try again from the beginning in such a case.

4. When subdivided into aliquots, keep fura-2/AM at below−20 °C in a tightly sealed box containing hygroscopic material to prevent moisture absorption during frequent use.

Preparation of glucose responsiveness experiment

1. Make KRB containing 1 mM Ca^{2+} as a superfusate during measurement. Make 100 ml of 0.1 M $CaCl_2$ stock solution to add Ca^{2+} to KRB. Prepare KRB containing 2.8 and 16.8 mM glucose.
2. Adjust pH of KRB stock solution to 7.3 with NaOH, because it will shift to 7.35–7.40 by the day of experiment.

Note: pH exceeding 7.4 may produce unsuccessful results.

BOX 2 | CONTINUED

3. Prepare tolbutamide in KRB by dissolving 1 M stock solution of tolbutamide (in DMSO) into KRB containing 2.8 mM glucose in a manner similar to that depicted in **Figure 3** (final concentration of tolbutamide, 200μM).

PROCEDURE

Measurement of $[Ca^{2+}]_i$ in response to glucose stimulation: *fura-2/AM loading* ● TIMING **30 min**

1. Prepare 10 ml of KRB (depending upon the total dead volume in the inlet tubing) containing 2.8 mM glucose and 1μM fura-2/AM for each culture dish.
2. Superfuse the islet cells with the fura-2/AM in KRB at a flow rate of 0.3 ml min^{-1} for 30 min at 37 °C.
3. Wash fura-2/AM solution with KRB containing 2.8 mM glucose at 37°C. This protocol is both easy and time saving. Indeed, because only islet cells strongly adhered to the glass bottom are left on the dish after the loading, cells of interest can be searched for using the microscope immediately after fura-2/AM loading, which contributes to obtaining responses from cells still in a healthy condition.
4. As an alternative to the above method of loading fura-2/AM by superfusion, fura-2/AM can be loaded by exchanging culture medium with KRB containing 2.8 mM glucose and 1 μM fura-2/AM, and incubated for 30 min at 37 °C in a humidified atmosphere containing 5% CO_2 (in a CO_2 incubator).

Measurement of $[Ca^{2+}]_i$ in response to glucose stimulation: $[Ca^{2+}]_i$ measurement ● TIMING **1 h**

5. Superfuse KRB containing 2.8 mM glucose. Start searching the area of interest without waiting additional post-loading minutes for the hydrolysis of AM residue, as the searching process is usually time consuming.
6. Capture transmitted light images of cells of interest.
7. Start imaging the ratio F340/F380. Fura-2 fluorescence is detected every 5 or 10 s at 500–520-nm wavelength following excitation at 340-nm (F340) and 380-nm (F380) wavelengths. The ratio image is obtained using an Argus 50. (See Troubleshooting section below.)
8. Exchange superfusate to KRB containing 16.8 mM glucose for 5–10 min and then return to KRB containing 2.8 mM glucose.
9. After the ratio recovers to baseline for about 10 min or so, check responsiveness of β-cells to tolbutamide by superfusing KRB containing 200 μM tolbutamide for a brief period within 30 s.

Measurement of 2-NBDG uptake ● TIMING **30–60 min**

10. After finishing Ca^{2+} imaging, start measurement of 2-NBDG uptake in a manner similar to that described for MIN6 cells. To discriminate β-cells from other cell types, KRB containing 200μM 2-NBDG and 2.8 mM glucose is loaded for 1 min. Quenching of fura-2 fluorescence is not required since the 2-NBDG fluorescence is strong enough in comparison with fura-2 fluorescence, and the 2-NBDG uptake is evaluated by the relative increase in the fluorescence.

ANTICIPATED RESULTS

A raw example of measurement of $[Ca^{2+}]_i$ and subsequent 2-NBDG uptake in pancreatic islet cells is shown in **Figure 6**. After loading fura-2/AM by superfusion, a region of interest is selected and a transmitted light image is captured (**Fig. 6a**). Cells to be monitored are then selected on the fluorescent image (**Fig. 6b**). Information on the $[Ca^{2+}]_i$ response to glucose stimulation (**Fig. 6c**) and the subsequent uptake of 2-NBDG by a brief superfusion (**Fig. 6d,e**) were used to evaluate the divergent uptake of heterogeneous islet cells in combination with later immunocytochemistry (**Fig. 6f**). Since islet cells consist of a heterogeneous population of cells, including glucose-responsive insulin-secreting β-cells and glucose-unresponsive glucagon-secreting α-cells as well as somatostatin-secreting δ-cells, later immunocytochemical identification of cell type is essential (see **Box 3**).

TROUBLESHOOTING

Problem: Extraordinary large ratio in $[Ca^{2+}]_i$ imaging.

Possible reason: Unhealthy cells may show a large ratio. Especially important, islet cells do not remain healthy for many hours in KRB containing 2.8 mM glucose. In addition, care should be taken to prevent high-temperature degradation of the coating materials of the emission filter, which can be continuously exposed to heat radiation from the xenon lamp during the experiment despite the heat-insulating lens.

Solution: Carry out experiments using freshly prepared cells. To retard degradation of the coating materials of the filter, empty the home filter position and use two heat-insulating lenses in the pathway from the lamp. The condition of the filters should be checked by making a calibration curve for $[Ca^{2+}]_i$.

▲ CRITICAL STEP A toothpick and a small bent spatula can be used to spread the grease and press the plate, respectively. If you use too much grease, it comes out from the gap between the dish and the plate and interferes with medium flow. If you use too little, the superfusate leaking into the gap will interfere with smooth exchange of the superfusate during drug application, which is especially problematic when high concentrations of 2-NBDG are applied.

3| Cover the central part of the oval glass bottom with a square cover glass with a small amount of vacuum grease (**Fig. 2**).

4| Mount the dish on the plastic holder on the inverted microscope stage and start superfusion immediately with KRB containing 5.6 mM glucose. Paint a small mark on the rim of the dish so that it coincides with the mark on the holder. This makes it possible to reproduce the angle of the dish when immunocytochemistry is conducted later.

BOX 3 | IMMUNOCYTOCHEMICAL IDENTIFICATION OF ISLET CELLS AFTER MEASUREMENT OF 2-[*N*-(7-NITROBENZ-2-OXA-1,3-DIAZOL-4-YL)AMINO]-2-DEOXY-D-GLUCOSE (2-NBDG) UPTAKE

REAGENTS

- Guinea pig anti-swine insulin antibody (Dako, cat. no. N1542)
- Rabbit anti-pig glucagon antibody (Dako, cat. no. L1813)
- Rhodamine-conjugated goat anti-guinea pig IgG (Chemicon)
- Rhodamine-conjugated goat anti-rabbit IgG (Cappel)
- Sodium phosphate buffer (PB)
- Paraformaldehyde (Nakalai)

EQUIPMENT

- Dichroic mirrors and filters: Nikon DM575 (EX 510–560, BA 590 LP)

Immunocytochemistry ● TIMING 5 h–4.5 d

1. At the end of the measurement of 2-NBDG uptake, capture transmitted light images of the analyzed cells at ×20, ×10, ×4 and ×2 for immunocytochemical identification of their location. Low-magnification lenses are especially convenient for finding the analyzed region in reference to the scratches previously made under the glass bottom of the culture dish.
2. Fix cells in cold 0.1 M PB containing 2% paraformaldehyde overnight at 4°C. Alternatively, pour the cold fixative on the cells and leave cells for up to 1 h at room temperature.
3. Wash three times (rotate the dish gently and wait for 5 min between each washing) with 0.01 M PBS. Cells may be treated with 1% BSA.
4. React cells with primary antibodies, such as guinea pig anti-pig insulin antibody (1:100) or rabbit anti-pig glucagon antibody (prediluted), at room temperature for 1 h or at 4 °C overnight.

Note: Can be left up to 3 d at 4 °C.

5. React with rhodamine-conjugated secondary antibody (1:100–1:500) at room temperature for 1 h.
6. Wash three times with PBS.
7. Mount the dish on the plastic holder on the microscope stage so that the mark on the rim of the dish coincides with the mark on the holder.
8. Show the previous low-magnification image of the cells on the PC monitor and affix tiny triangles made of opaque tape on both ends of individual major scratches observed on the monitor screen. Then find the same scratch pattern by microscope and adjust the field of view so that the identical pattern is seen on the monitor using the opaque triangles as guides. Finer adjustment can be made by comparing the current image with the previous image. Repeat the process in higher-magnification views.
9. Examine rhodamine fluorescence.

ANTICIPATED RESULTS

See **Figure 6f**.

Measurement of 2-NBDG uptake ● TIMING 30–60 min

5| Select area of interest and capture a transmitted light image.

6| Demarcate cells. Select an area for evaluating changes in background fluorescence.

7| Adjust the gain of the detection system and capture fluorescent images. A transmitted light image with no ND filter is useful for identifying locations of cells on the monitor screen by the intrinsic fluorescence of the cells. Strong ND filters are used when the fluorescence of cells is saturated after loading 2-NBDG.

8| Superfuse MIN6 cells with glucose-free KRB for 15 min.

9| Change superfusate to D-glucose-free KRB containing 50–600 μM 2-NBDG for 15–120 s, and then wash.

▲ CRITICAL STEP The concentration of 2-NBDG and the loading period are to be determined according to the purpose of the experiment, the type of GLUTs of interest and the signal-to-noise ratio of the detection system. For the signal-to-noise ratio and the superfusion technique used in the present system, the shortest practical loading period is 15 s, and the smallest concentration is 50 μM. When 600 μM 2-NBDG is used, a loading period longer than 120 s should be avoided because of the nonlinear increase in the 2-NBDG fluorescence over time[9]. With a system requiring a long loading period (e.g., tens of minutes),

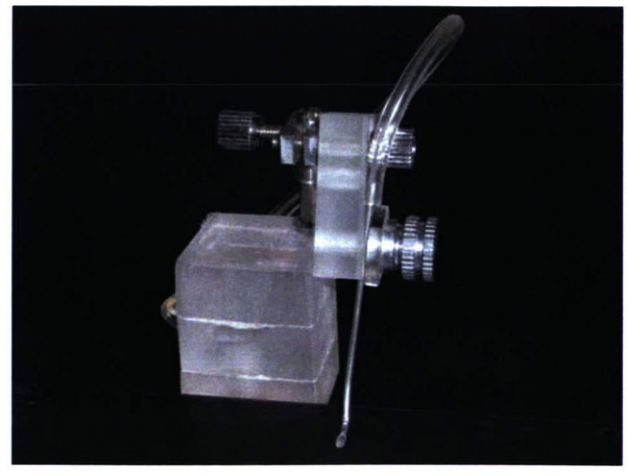

Figure 4 | A custom-made holder for the outlet needle (Narishige). Height, rotation angle and lean angle of the needle are freely adjustable without using a screwdriver.

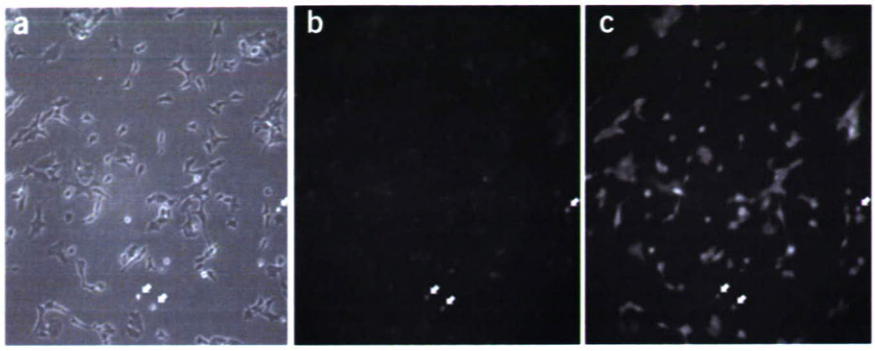

Figure 5 | Measurement of 2-[*N*-(7-nitrobenz-2-oxa-1,3-diazol-4-yl)amino]-2-deoxy-D-glucose (2-NBDG) uptake into MIN6 cells. (**a**) Transmitted light image (×20). Arrows indicate debris of dead cells. Raw fluorescent images measured at 540-nm wavelength with no neutral density (ND) filter (**b**) before and (**c**) after loading Krebs Ringer bicarbonate buffer (KRB) containing 600 μM 2-NBDG for 15 s. Note that no increase in the fluorescence intensity is seen for the debris (arrows). The field of view in the fluorescent images (**b**) and (**c**) was narrowed by the diaphragm in the fluorescent light path.

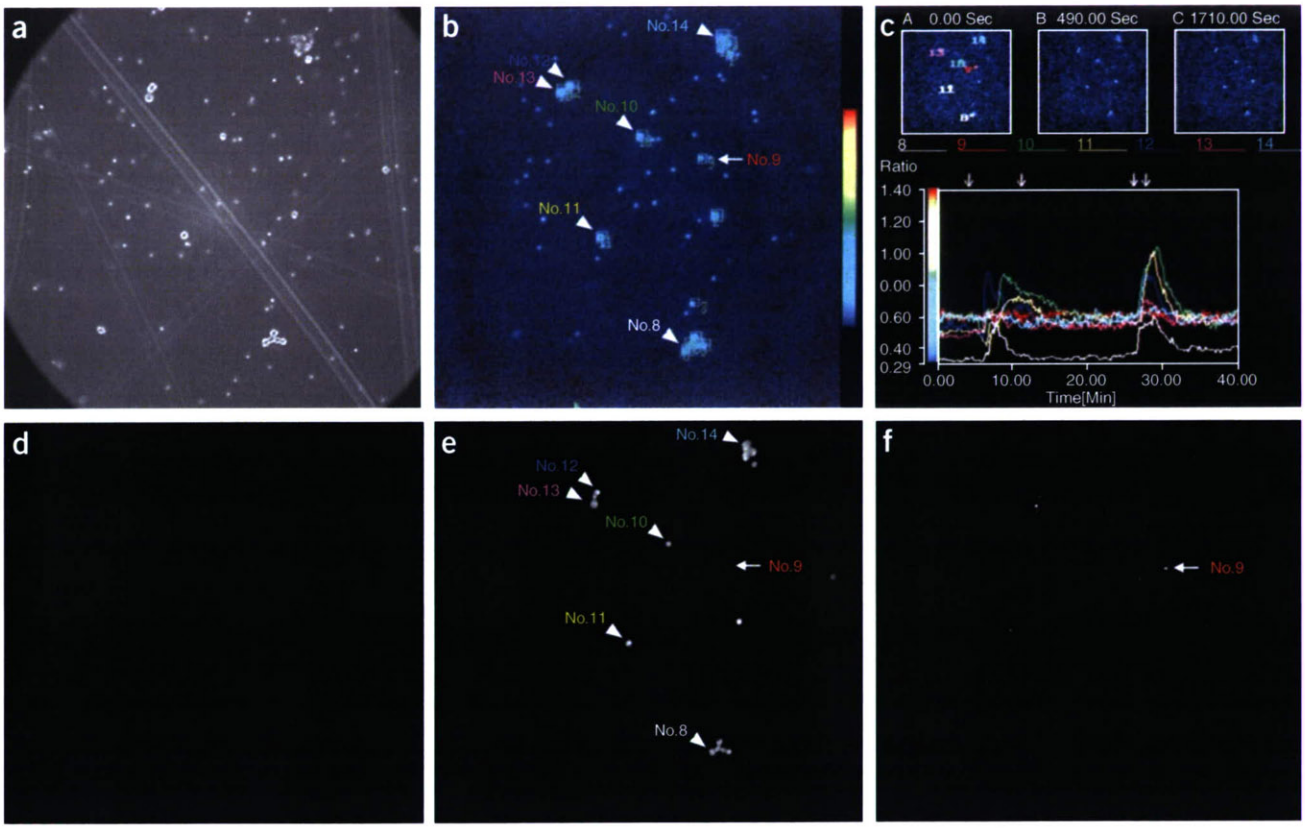

Figure 6 | Measurement of $[Ca^{2+}]_i$ in response to glucose stimulation and subsequent 2-[*N*-(7-nitrobenz-2-oxa-1,3-diazol-4-yl)amino]-2-deoxy-D-glucose (2-NBDG) uptake in living pancreatic islet cells followed by immunocytochemical identification. (**a**) Transmitted light image (×20). Scratches made under the glass bottom of the dish are visible. (**b**) Raw fluorescent image examined at 500–520-nm wavelength for 380-nm excitation after loading of 1 μM fura-2/AM by superfusion. Areas demarcated by squares were tentatively selected for monitoring $[Ca^{2+}]_i$ responses before starting the measurement. Of these, the responses of cells indicated by colored numbers are exemplified (see below). (**c**) A window of the Argus 50 for $[Ca^{2+}]_i$ analysis. Seven areas can be analyzed on one page of the Argus 50 (seven colors are assigned automatically). Areas showing increases (no. 8 and nos. 10–14) and no increase (no. 9) in $[Ca^{2+}]_i$ are expressed as the change in fura-2 fluorescence ratio (340 or 380 nm) (lower panel). Small downward arrows above the lower panel indicate periods of superfusing Krebs Ringer bicarbonate buffer (KRB) containing 16.8 mM glucose (between the two left arrows) and 200 μM tolbutamide (between the right arrows). The response times to tolbutamide coincided for cells responding to high glucose, whereas the response times to glucose varied, indicating accuracy of the superfusion and differences in intracellular metabolism after glucose uptake among cells. Upper insets are provided by the software for checking locations of cells and changes in the fluorescence at different time points. Fluorescent images measured at 540-nm wavelength (**d**) before and (**e**) after loading 200 μM 2-NBDG for 1 min. Cells incorporating 2-NBDG are β-cells[9], and uptake of 2-NBDG into cell no. 9 was undetectable during 1 min loading. (**f**) Immunocytochemistry of glucagon. Rhodamine-conjugated secondary antibody was used. Cell no. 9 (arrow) was clearly immunopositive for glucagon. Rhodamine fluorescence was examined with a 590-nm longpass filter (excitation wavelength 510–560 nm). Note that the location of the cells incorporating abundant 2-NBDG can be identified by their vague fluorescence. In (**a**–**e**), cells were superfused continuously with KRB containing 2.8 mM glucose at 37 °C, and the KRB was supplemented as indicated. In these original pictures, no subtraction or shading correction was done. Contrast was adjusted for clarity only in panels (**d**) and (**e**). Note that some cells were lost and some not seen in the original transmitted light image entered from upstream during superfusion. Some of these data were first published in ref. 9.

some investigators use a very low concentration of 2-NBDG (10μM)[13]. For a long loading period, time-dependent extinction should also be considered. In MIN6 cells, the intensity of 2-NBDG fluorescence (200μM loaded for 60 s) was linearly decreased to 87.7, 70.9 and 56.6% 15, 30 and 60 min after uptake, respectively, under dark condition (K. Yamada and N. Inagaki, unpublished data). Care should be taken that the actual loading period of 2-NBDG from the beginning of superfusion to complete washing is constant for all of the cells compared. Differences in the local temperature within the area of interest should be within 1°C (e.g., 36.5–37.5 °C) to minimize temperature-dependent variance of the uptake[9].

? TROUBLESHOOTING

10| When 2-NBDG uptake is evaluated in the presence of glucose, skip Step 8 and change the superfusate to KRB containing 2-NBDG and glucose. The glucose concentration added to the KRB should be determined according to the purpose of experiment. To test inhibition of 2-NBDG uptake by D-glucose, superfuse cells with KRB containing 11.2 mM D-glucose and compare the 2-NBDG uptake with that in the absence of D-glucose. The uptake of 2-NBDG (600μM loaded for 2 min) in the presence of 11.2 mM glucose was significantly inhibited by 52.5 ± 6.3% compared with uptake in the absence of glucose[8].

11| After washing for 5 min, capture fluorescent images.

12| Calculate the relative fluorescence intensity of each cell before and after loading 2-NBDG by subtracting the corresponding background fluorescence from the fluorescence intensity of the cells.

13| Calculate the net increase in the fluorescence intensity for each cell by subtracting the relative fluorescence intensity before from that after loading 2-NBDG.

14| To test whether the 2-NBDG uptake occurs through GLUTs, superfuse cells with KRB containing 10μM cytochalasin B 5 min before the 2-NBDG loading. In MIN6 cells, the increase in fluorescence by loading 200μM 2-NBDG for 15 s was almost completely inhibited in the presence of cytochalasin B[9].

? TROUBLESHOOTING

Troubleshooting advice can be found in **Table 1**.

TABLE 1 | Troubleshooting table.

Step	Problem	Possible reasons	Solution
9	Variable results in 2-[*N*-(7-nitrobenz-2-oxa-1,3-diazol-4-yl)amino]-2-deoxy-D-glucose (2-NBDG) fluorescence in quantitative measurements or high background fluorescence due to 2-NBDG	Unstable superfusion in the chamber	Check for smooth superfusion by dropping a small amount of dye such as pontamine sky blue (Brilliant Blue 6B, CI-24420, Tokyo Chemical Industry, Tokyo, Japan) using an extra dish without cells. Adjust the position of the outlet needle so that it slightly protrudes into the glass bottom part. Adjust the inlet angle and direction finely so that a smooth, laminar flow is obtained. A constant sound of sucking of the superfusate from the outlet needle indicates a stable flow. Measure the temperature of each region of interest with a thin thermistor probe to confirm that the temperature difference is within 1 °C. An area meeting this criterion can be marked on the cover glass. Measurement of the local temperature also helps in finding irregular flow
		Pollution by 2-NBDG fluorescence from the forceps used for placing and removing the plastic plate on the glass-bottom culture dish, or other materials such as the thermistor probe	Every time a dish is exchanged, the plate and forceps used should be rinsed thoroughly. Make several additional plates to save time. Each time vacuum grease is taken from the tube, use a new disposable toothpick so that the grease itself is not polluted by 2-NBDG fluorescence. Similar care should be taken for other parts
		Variance of uptake specific to the particular cell types of interest	See ANTICIPATED RESULTS

ANTICIPATED RESULTS

An example of the raw measurements of 2-NBDG uptake in MIN6 cells is shown in **Figure 5**. The fluorescence of MIN6 cells, which was only slightly discernible before loading, was remarkably increased by a brief (15 s) superfusion of 600μM 2-NBDG in the absence of glucose. In the transmitted light image, cells with an abnormal round shape are easily distinguished from normal cells exhibiting irregular shape[24]. Abnormal cells and areas where multiple cells are overlapping are to be excluded from the

analysis. MIN6 cells exhibit a relatively homogeneous uptake of 2-NBDG. However, when other cell types are used, care should be taken to determine whether the variable uptake of 2-NBDG is due to intrinsic differences in the glucose uptake of individual cells (**Box 2**, **Box 3** and **Fig. 6**).

ACKNOWLEDGMENTS We are grateful to our collaborators, Drs. Masanori Nakata and Naoki Horimoto. We also thank Drs. K. Yoshizaki and S. Sato for technical help, and Dr. J. Miyazaki (Osaka University) for providing us with MIN6 cells.

COMPETING INTERESTS STATEMENT The authors declare no competing financial interests.

Published online at http://www.natureprotocols.com
Reprints and permissions information is available online at http://npg.nature.com/reprintsandpermissions

1. Sokoloff, L. Sites and mechanisms of function-related changes in energy metabolism in the nervous system. *Dev. Neurosci.* **15**, 194–206 (1993).
2. Heimberg, H., De Vos, A., Pipeleers, D., Thorens, B. & Schuit, F. Differences in glucose transporter gene expression between rat pancreatic a- and b-cells are correlated to differences in glucose transport but not in glucose utilization. *J. Biol. Chem.* **270**, 8971–8975 (1995).
3. Sokoloff, L. *et al.* The [^{14}C]deoxyglucose method for the measurement of local cerebral glucose utilization: theory, procedure, and normal values in the conscious and anesthetized albino rat. *J. Neurochem.* **28**, 897–916 (1977).
4. Turkheimer, F. *et al.* The use of spectral analysis to determine regional cerebral glucose utilization with positron emission tomography and [^{18}F]fluorodeoxyglucose: theory, implementation, and optimization procedures. *J. Cereb. Blood Flow Metab.* **14**, 406–422 (1994).
5. Dienel, G.A., Cruz, N.F., Adachi, K., Sokoloff, L. & Holden, J.E. Determination of local brain glucose level with [^{14}C]methylglucose: effects of glucose supply and demand. *Am. J. Physiol.* **273**, E839–E849 (1997).
6. Axelrod, J.D. & Pilch, P.F. Unique cytochalasin B binding characteristics of the hepatic glucose carrier. *Biochemistry* **22**, 2222–2227 (1983).
7. Yoshioka, K. *et al.* A novel fluorescent derivative of glucose applicable to the assessment of glucose uptake activity of *Escherichia coli*. *Biochim. Biophys. Acta* **1289**, 5–9 (1996).
8. Matsuoka, H. *et al.* Viable cell detection by the combined use of fluorescent glucose and fluorescent glycine. *Biosci. Biotechnol. Biochem.* **67**, 2459–2462 (2003).
9. Yamada, K. *et al.* Measurement of glucose uptake and intracellular calcium concentration in single, living pancreatic β-cells. *J. Biol. Chem.* **275**, 22278–22283 (2000).
10. Miyazaki, J. *et al.* Establishment of a pancreatic beta cell line that retains glucose-inducible insulin secretion: special reference to expression of glucose transporter isoforms. *Endocrinology* **127**, 126–132 (1990).
11. Lloyd, P.G., Hardin, C.D. & Sturek, M. Examining glucose transport in single vascular smooth muscle cells with a fluorescent glucose analogue. *Physiol. Res.* **48**, 401–410 (1999).
12. Roman, Y., Alfonso, A., Carmen Louzao, M., Vieytes, M.R. & Botana, L.M. Confocal microscopy study of the different patterns of 2-NBDG uptake in rabbit enterocytes in the apical and basal zone. *Eur. J. Physiol.* **443**, 234–239 (2001).
13. Ball, S.W., Bailey, J.R., Stewart, J.M., Vogels, C.M. & Westcott, S.A. A fluorescent compound for glucose uptake measurements in isolated rat cardiomyocytes. *Can. J. Physiol. Pharmacol.* **80**, 205–209 (2002).
14. Loaiza, A., Porras, O.H. & Barros, L.F. Glutamate triggers rapid glucose transport stimulation in astrocytes as evidenced by real-time confocal microscopy. *J. Neurosci.* **23**, 7337–7342 (2003).
15. Bernardinelli, Y., Magistretti, P.J. & Chatton, J.-Y. Astrocytes generate Na-mediated metabolic waves. *Proc. Natl. Acad. Sci. USA* **101**, 14937–14942 (2004).
16. Porras, O.H., Loaiza, A. & Barros, F. Glutamate mediates acute glucose transport inhibition in hippocampal neurons. *J. Neurosci.* **24**, 9669–9673 (2004).
17. Itoh, Y., Abe, T., Takaoka, R. & Tanahashi, N. Fluorometric determination of glucose utilization in neurons *in vitro* and *in vivo*. *J. Cereb. Blood Metab.* **24**, 993–1003 (2004).
18. Blomstrand, F. & Giaume, C. Kinetics of endothelin-induced inhibition and glucose permeability of astrocyte gap junctions. *J. Neurosci. Res.* **83**, 996–1003 (2006).
19. O'Neil, R.G., Wu, L. & Mullani, N. Uptake of a fluorescent deoxyglucose analogue (2-NBDG) in tumor cells. *Mol. Imaging Biol.* **7**, 388–392 (2005).
20. Cheng, Z. *et al.* Near-infrared fluorescent deoxyglucose analogue for tumor optical imaging in cell culture and living mice. *Bioconjug. Chem.* **17**, 662–669 (2006).
21. Nakata, M. *et al.* Effects of statins on the adipocyte maturation and expression of glucose transporter 4 (SLC2A4): implications in glycaemic control. *Diabetologia* **49**, 1881–1892 (2006).
22. Zou, C., Wang, Y. & Shen, Z. 2-NBDG as a fluorescent indicator for direct glucose uptake measurement. *J. Biochem. Biophys. Methods* **64**, 207–215 (2005).
23. Yoshioka, K. *et al.* Intracellular fate of 2-NBDG, a fluorescent probe for glucose uptake activity, in *Escherichia coli* cells. *Biosci. Biotech. Biochem.* **60**, 1899–1901 (1996).
24. Minami, K. *et al.* Insulin secretion and differential gene expression in glucose-responsive and -unresponsive MIN6 sublines. *Am. J. Physiol. Endocrinol. Metab.* **279**, E773–E781 (2000).
25. Yada, T., Itoh, K. & Nakata, M. Glucagon-like peptide-1-(7-36)amide and a rise in cyclic adenosine 3,5-monophosphate increase cytosolic free Ca^{2+} in rat pancreatic beta-cells by enhancing Ca^{2+} channel activity. *Endocrinology* **133**, 1685–1692 (1993).

Available online at www.sciencedirect.com
ScienceDirect
Journal of Controlled Release 119 (2007) 136–141
journal of controlled release
www.elsevier.com/locate/jconrel

Efficient gene transfer into murine pancreatic islets using adenovirus vectors

Eri Mukai [a,b], Shimpei Fujimoto [c], Fuminori Sakurai [a], Kenji Kawabata [a], Manabu Yamashita [a,b], Nobuya Inagaki [c], Hiroyuki Mizuguchi [a,d,*]

[a] *Laboratory of Gene Transfer and Regulation, National Institute of Biomedical Innovation, 7-6-8 Saito, Asagi, Ibaraki, Osaka 567-0085, Japan*
[b] *Japan Health Sciences Foundation, Tokyo 103-0001, Japan*
[c] *Department of Diabetes and Clinical Nutrition, Graduate School of Medicine, Kyoto University, Kyoto 606-8507, Japan*
[d] *Graduate School of Pharmaceutical Sciences, Osaka University, Osaka 565-0871, Japan*

Received 14 October 2006; accepted 21 January 2007
Available online 31 January 2007

Abstract

We investigated the efficiency of gene transduction into murine pancreatic islets using the adenovirus (Ad) vector. Western blotting analysis showed that mouse pancreatic islets express coxsackievirus and adenovirus receptor, a receptor for Ad. Nevertheless, gene expression after transduction of the Ad vector *in vitro* was observed only in the periphery of the islets, probably due to physical obstruction against Ad infection of the cells in the inside of islets. Ca^{2+}-free treatment before the Ad vector transduction enhanced transduction efficiency in the islets, but not the cells in the inside of islets. The Ad vector transduction through the celiac artery *in vivo* and then cultivation of islets *in vitro* resulted in efficient transduction even in the inside of islets. Thus we propose a new strategy for efficient gene transfer to pancreatic β-cells.

Keywords: Adenovirus vector; Pancreatic islets; β-cells; Gene transduction

1. Introduction

A technique for efficient gene transfer to pancreatic islets provides a valuable tool not only for basic research for insulin-secreting β-cells, but also for an approach to gene therapy for diabetes mellitus. Type 1 diabetes mellitus is an autoimmune disease in which pancreatic β-cells are almost destroyed, and pancreatic islet transplantation has been validated as an ideal therapy for type 1 diabetes [1–3]. However, this treatment has some problems, including a donor shortage and a lack of efficient techniques to maintain functional islet mass. Type 2 diabetes, caused by complicated factors including heredity and diet, leads to impairment of insulin secretion from pancreatic β-cells and lowered insulin sensitivity in liver, muscle, and adipose tissue [4,5]. For an amelioration of insulin secretion from pancreatic β-cells, a permanent normalization of islet function is essential, and new strategies for a treatment of the disease have been required.

There are several types of vectors available for gene transfer to different cell types. Non-viral vectors, such as lipofection and electroporation, have been used for gene transfer, but their use leads to low transduction efficiency in pancreatic islets [6–9]. On the other hand, viral vectors are attractive vehicles for gene transfer because of highly efficient gene transduction. Adenovirus (Ad) vectors are the most readily available vectors currently, because they are relatively easy to construct, can be produced at high titers, and have high transduction efficiencies [10,11]. Ad vectors have been studied for gene transfer to pancreatic β-cells [12–16], but a technique for efficient gene transfer to β-cells, especially in a condition that islet cluster is retained without a treatment of single cell preparation, has not been established. A pancreatic islet is a cluster of several kinds of endocrine cells located uniquely and in an established order; for example, β-cells occupy the inner area of islet. The aggregation and orderly location of these endocrine cells seem to be important for regulatory hormone secretion from each endocrine cell.

In the present study, we investigated the efficiency of Ad vector-mediated gene transduction into isolated pancreatic

* Corresponding author. Laboratory of Gene Transfer and Regulation, National Institute of Biomedical Innovation, 7-6-8 Saito, Asagi, Ibaraki, Osaka 567-0085, Japan. Tel.: +81 72 641 9815; fax: +81 72 641 9816.
E-mail address: mizuguch@nibio.go.jp (H. Mizuguchi).

0168-3659/$ - see front matter © 2007 Elsevier B.V. All rights reserved.
doi:10.1016/j.jconrel.2007.01.012